
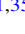








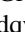









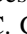

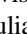


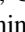
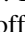








Gaia17biu/SN 2017egm in NGC 3191: The Closest Hydrogen-poor Superluminous Supernova to Date Is in a “Normal,” Massive, Metal-rich Spiral Galaxy

Subhash Bose^{1,35} , Subo Dong^{1,35} , A. Pastorello², Alexei V. Filippenko^{3,4,36} , C. S. Kochanek^{5,6} , Jon Mauerhan³ , C. Romero-Cañizales^{7,8} , Thomas G. Brink³, Ping Chen¹, J. L. Prieto^{7,8} , R. Post⁹, Christopher Ashall¹⁰, Dirk Grupe¹¹ , L. Tomasella², Stefano Benetti², B. J. Shappee^{12,37,38} , K. Z. Stanek^{5,6}, Zheng Cai¹³ , E. Falco¹⁴ , Peter Lundqvist¹⁵ , Seppo Mattila¹⁶, Robert Mutel¹⁷ , Paolo Ochner^{2,18}, David Pooley¹⁹ , M. D. Stritzinger²⁰ , S. Villanueva, Jr.⁵ , WeiKang Zheng³, R. J. Beswick²¹, Peter J. Brown²² , E. Cappellaro² , Scott Davis¹⁰, Morgan Fraser²³ , Thomas de Jaeger³ , N. Elias-Rosa², C. Gall²⁴ , B. Scott Gaudi⁵ , Gregory J. Herczeg¹ , Julia Hestenes³, T. W.-S. Holoiien^{5,6,39} , Griffin Hosseinzadeh^{25,26} , E. Y. Hsiao¹⁰ , Shaoming Hu²⁷ , Shin Jaejin²⁸, Ben Jeffers³, R. A. Koff²⁹, Sahana Kumar¹⁰, Alexander Kurtenkov³⁰, Marie Wingyee Lau¹³ , Simon Prentice³¹, T. Reynolds¹⁶, Richard J. Rudy³², Melissa Shahbandeh¹⁰, Auni Somero¹⁶, Keivan G. Stassun³³ , Todd A. Thompson^{5,6}, Stefano Valenti³⁴ , Jong-Hak Woo²⁸ , and Sameen Yunus³

¹ Kavli Institute for Astronomy and Astrophysics, Peking University, Yi He Yuan Road 5, Hai Dian District, Beijing 100871, People's Republic of China

² INFN-Osservatorio Astronomico di Padova, Vicolo dell'Osservatorio 5, I-35122 Padova, Italy

³ Department of Astronomy, University of California, Berkeley, CA 94720-3411, USA

⁴ Miller Institute for Basic Research in Science, University of California, Berkeley, CA 94720, USA

⁵ Department of Astronomy, The Ohio State University, 140 West 18th Avenue, Columbus, OH 43210, USA

⁶ Center for Cosmology and AstroParticle Physics (CCAPP), The Ohio State University, 191 W. Woodruff Avenue, Columbus, OH 43210, USA

⁷ Millennium Institute of Astrophysics, Santiago, Chile

⁸ Núcleo de Astronomía de la Facultad de Ingeniería y Ciencias, Universidad Diego Portales, Av. Ejército 441, Santiago, Chile

⁹ Post Observatory, Lexington, MA 02421, USA

¹⁰ Department of Physics, Florida State University, 77 Chieftain Way, Tallahassee, FL 32306, USA

¹¹ Department of Earth and Space Science, Morehead State University, 235 Martindale Dr., Morehead, KY 40351, USA

¹² Carnegie Observatories, 813 Santa Barbara Street, Pasadena, CA 91101, USA

¹³ UCO/Lick Observatory, University of California at Santa Cruz, Santa Cruz, CA 95064, USA

¹⁴ Harvard-Smithsonian Center for Astrophysics, 60 Garden Street, Cambridge, MA 02138, USA

¹⁵ Department of Astronomy and The Oskar Klein Centre, AlbaNova University Center, Stockholm University, SE-10691 Stockholm, Sweden

¹⁶ Tuorla Observatory, Department of Physics and Astronomy, University of Turku, Väisäläntie 20, FI-21500 Piikkiö, Finland

¹⁷ Department of Physics and Astronomy, University of Iowa, USA

¹⁸ Dipartimento di Fisica e Astronomia, Università di Padova, via Marzolo 8, I-35131 Padova, Italy

¹⁹ Trinity University, Department of Physics & Astronomy, One Trinity Place, San Antonio, TX 78212, USA

²⁰ Department of Physics and Astronomy, Aarhus University, Ny Munkegade 120, DK-8000 Aarhus C, Denmark

²¹ Jodrell Bank Centre for Astrophysics & e-MERLIN, School of Physics and Astronomy, The University of Manchester, Manchester, M13 9PL, UK

²² George P. and Cynthia Woods Mitchell Institute for Fundamental Physics & Astronomy, Texas A. & M. University, Department of Physics and Astronomy, 4242 TAMU, College Station, TX 77843, USA

²³ School of Physics, O'Brien Centre for Science North, University College Dublin, Belfield, Dublin 4, Ireland

²⁴ Dark Cosmology Centre, Niels Bohr Institute, University of Copenhagen, Juliane Maries Vej 30, DK-2100 Copenhagen, Denmark

²⁵ Las Cumbres Observatory, 6740 Cortona Drive, Ste. 102, Goleta, CA 93117-5575, USA

²⁶ Department of Physics, University of California, Santa Barbara, CA 93106-9530, USA

²⁷ Shandong Provincial Key Laboratory of Optical Astronomy and Solar-Terrestrial Environment, Institute of Space Sciences, Shandong University, Weihai 264209, People's Republic of China

²⁸ Astronomy Program, Department of Physics and Astronomy, Seoul National University, Seoul, 151-742, Republic of Korea

²⁹ Antelope Hills Observatory, 980 Antelope Drive West, Bennett, CO 80102, USA

³⁰ Institute of Astronomy and NAO, Bulgarian Academy of Sciences, 72 Tsarigradsko Shose Blvd., 1784 Sofia, Bulgaria

³¹ Astrophysics Research Institute, Liverpool John Moores University, Liverpool, L3 5RF, UK

³² Space Science Applications Laboratory, The Aerospace Corporation, Mail Stop: M2-266, P.O. Box 92957, Los Angeles, CA 90009-2957, USA

³³ Department of Physics & Astronomy, Vanderbilt University, 6301 Stevenson Center Lane, Nashville, TN 37235, USA

³⁴ Department of Physics, University of California, Davis, CA 95616, USA

Received 2017 August 2; revised 2017 December 14; accepted 2017 December 14; published 2018 January 23

Abstract

Hydrogen-poor superluminous supernovae (SLSNe-I) have been predominantly found in low-metallicity, star-forming dwarf galaxies. Here we identify Gaia17biu/SN 2017egm as an SLSN-I occurring in a “normal” spiral galaxy (NGC 3191) in terms of stellar mass (several times $10^{10} M_{\odot}$) and metallicity (roughly solar). At redshift $z = 0.031$, Gaia17biu is also the lowest-redshift SLSN-I to date, and the absence of a larger population of SLSNe-I in dwarf galaxies of similar redshift suggests that metallicity is likely less important to the production of SLSNe-I than previously believed. With the smallest distance and highest apparent brightness for an SLSN-I, we are able to study Gaia17biu in unprecedented detail. Its pre-peak near-ultraviolet to optical color is similar to that of

³⁵ Corresponding authors: Subo Dong (dongsubo@pku.edu.cn), Subhash Bose (email@subhashbose.com).

³⁶ Miller Senior Fellow.

³⁷ Hubble Fellow.

³⁸ Carnegie-Princeton Fellow.

³⁹ US Department of Energy Computational Science Graduate Fellow.

Gaia16apd and among the bluest observed for an SLSN-I, while its peak luminosity ($M_g = -21$ mag) is substantially lower than that of Gaia16apd. Thanks to the high signal-to-noise ratios of our spectra, we identify several new spectroscopic features that may help to probe the properties of these enigmatic explosions. We detect polarization at the $\sim 0.5\%$ level that is not strongly dependent on wavelength, suggesting a modest, global departure from spherical symmetry. In addition, we put the tightest upper limit yet on the radio luminosity of an SLSN-I with $< 5.4 \times 10^{26}$ erg s $^{-1}$ Hz $^{-1}$ at 10 GHz, which is almost a factor of 40 better than previous upper limits and one of the few measured at an early stage in the evolution of an SLSN-I. This limit largely rules out an association of this SLSN-I with known populations of gamma-ray-burst-like central engines.

Key words: galaxies: individual (NGC 3191) – supernovae: general – supernovae: individual (SN 2017egm, Gaia17biu)

Supporting material: data behind figures

1. Introduction

The first hydrogen-poor (i.e., Type I) superluminous supernova (SLSN-I), SN 2005ap, was discovered a dozen years ago by the Texas Supernova Search, a wide-field, untargeted survey for supernovae (SNe) with a high level of spectroscopic completeness (Quimby et al. 2007). Subsequent, largely untargeted, surveys have established the existence of SLSNe-I as a distinct class of SN (Quimby et al. 2011). SLSNe-I are among the least understood SN populations. The explosion mechanism and energy supply mechanism responsible for their extreme peak luminosities ($M_{\text{peak}} \lesssim -21$ mag) and radiated energies are debated (Gal-Yam 2012), and there are no identifications of progenitor stars.

The host of SN 2005ap was a low-metallicity, star-forming dwarf galaxy, which is true of almost all subsequent examples of SLSNe (see, e.g., Neill et al. 2011; Quimby et al. 2011; Stoll et al. 2011; Chen et al. 2013; Lunnan et al. 2014; Leloudas et al. 2015b; Perley et al. 2016; hereafter P16). There are exceptions, such as PTF10uhf (P16) and ASASSN-15lh (Dong et al. 2016), which are both in higher-mass and higher-metallicity galaxies, although the nature of ASASSN-15lh is debated (Leloudas et al. 2016; Godoy-Rivera et al. 2017). The underrepresentation of dwarf galaxies in most galaxy-targeted, professional surveys (e.g., Leaman et al. 2011) and in amateur SN searches (see, e.g., Holoien et al. 2017a) would then explain why SLSNe-I were discovered only recently. This has also led to the hypothesis that low metallicity may be required for the production of SLSNe-I (see, e.g., P16; Schulze et al. 2018; Chen et al. 2017b; hereafter C17). On the other hand, the more local SN searches may simply have missed SLSNe-I owing to their rarity, as their rate is about three orders of magnitude lower than that of normal Type Ia SNe (Quimby et al. 2013; McCrum et al. 2015; Prajs et al. 2017). As an added consequence of their scarcity, few SLSNe-I have been found at sufficiently low redshifts to permit detailed multiwavelength studies (Brown et al. 2016; Dong et al. 2016; Nicholl et al. 2016; Godoy-Rivera et al. 2017; Kangas et al. 2017; Yan et al. 2017).

The explosion mechanism of SLSNe is highly debated, and their extreme luminosities cannot be explained as conventional SNe. Several possible mechanisms have been proposed to explain the powering source, among which the magnetar-spindown (e.g., Kasen & Bildsten 2010), pair-instability SNe (PISNe; e.g., Woosley et al. 2007), and ejecta-circumstellar material (CSM) interactions (e.g., Blinnikov & Sorokina 2010; Sorokina et al. 2016) being the most commonly discussed.

Owing to the perceived preference of SLSNe-I to occur in low-metallicity and dwarf galaxies, it has also been proposed (Lunnan et al. 2014; Angus et al. 2016) that SLSNe-I may be

powered by a central engine similar to those in long-duration gamma-ray bursts (GRBs), which are also preferentially found in such hosts (Stanek et al. 2006).

Early spectra of SLSNe-I show a characteristic W-shaped feature near ~ 4200 Å that is composed of a pair of broad absorption features associated with O II (Pastorello et al. 2010; Quimby et al. 2011). SLSNe-I spectroscopically fall under the classification of SNe Ic due to the absence of any hydrogen, helium, or silicon. However, early spectra of SLSNe-I are significantly different than the features exhibited by SNe Ic, most notably the W-shaped oxygen feature. The photometric and spectroscopic evolution and late-time energy sources are also significantly different between these two SN classes. However, in many cases, their spectra start to show similarities to SNe Ic as the spectra evolve (e.g., SN 2010gx; Pastorello et al. 2010).

Here we identify Gaia17biu (also known as SN 2017egm) as a SLSN-I (Dong et al. 2017), and we discuss its discovery and classification in Section 2. The host galaxy, NGC 3191 (see Figure 1), is unusually massive and metal-rich, as we discuss in Section 3. With a redshift $z = 0.03063$ (SDSS Collaboration et al. 2017), it is the closest SLSN-I yet discovered, being a factor of two closer than the next-nearest example (PTF11hrq at $z = 0.057$; P16). This makes possible the intensive multiwavelength and spectroscopic observations of this SLSN-I presented in Section 4. We discuss the implications of Gaia17biu in Section 5. We adopt a luminosity distance of $D_L = 138.7 \pm 1.9$ Mpc assuming a standard *Planck* cosmology (Planck Collaboration et al. 2016) and foreground Galactic $R_V = 3.1$ extinction of $E(B - V) = 0.0097 \pm 0.0005$ mag (Schlafly & Finkbeiner 2011). The blue colors and the absence of narrow Na I D absorption indicates that there is little additional line-of-sight dust in the host galaxy.

2. Discovery and Classification

Gaia17biu ($\alpha = 10^{\text{h}}19^{\text{m}}05^{\text{s}}.62$, $\delta = 46^{\circ}27'14''.08$, J2000) was discovered by the Photometric Science Alerts Team of the *Gaia* mission (Delgado et al. 2017) on 2017 May 23, UT 21:41:13 (JD = 2,457,897.40), at 16.72 mag in the *Gaia* G band (UT dates and times are used throughout this paper), and its IAU designation is SN 2017egm. It was subsequently classified as a SN II by Xiang et al. (2017) based on a spectrum taken on 2017 May 26, although Xiang et al. (2017) noted that the object's luminosity (~ -19 mag) appeared to be abnormally bright for a SN II.

In particular, the source was detected in images taken by the All-Sky Automated Survey for SuperNovae (ASAS-SN; Shappee et al. 2014) starting on 2017 May 20 (JD = 2,457,893.76) at



Figure 1. *gri* false-color composite image of NGC 3191 with the presence of SN Gaia17biu observed on 2017 July 1 from NOT+ALFOSC is shown in the right panel. The pre-explosion SDSS image is at left with the SN location marked by a green box. Both image cutouts are $100'' \times 100''$ in size.

$V = 17.36 \pm 0.14$ mag (the light green open circles in Figure 3). The ASAS-SN collaboration, working with other groups, attempts to spectroscopically classify all SNe discovered or recovered by ASAS-SN in order to build an unbiased nearby SN sample with high spectroscopic completeness (e.g., Holoién et al. 2017a). In this case, the Nordic Optical Telescope (NOT) Unbiased Transient Survey (NUTS) collaboration⁴⁰ (Mattila et al. 2016) obtained a high signal-to-noise ratio (S/N) NOT Andalucía Faint Object Spectrograph and Camera (ALFOSC) spectrum on 2017 May 30. This spectrum, as well as a number of subsequent ones (see the top of Figure 6), showed broad, “W-shaped” O II absorption features at rest-frame ~ 4100 and ~ 4400 Å that are characteristic of most known SLSNe-I (Quimby et al. 2011). This led us to conclude that Gaia17biu was actually a SLSN-I (Dong et al. 2017). Later, Nicholl et al. (2017) duplicated our already public finding.

3. The Host Galaxy

As pointed out by Dong et al. (2017), the host galaxy of Gaia17biu, NGC 3191, is atypical for known SLSN-I hosts. It is massive, and it is correspondingly relatively metal-rich, in accord with the well-established mass–metallicity relation (e.g., Tremonti et al. 2004). Kelly & Kirshner (2012) analyzed Sloan Digital Sky Survey (SDSS) photometry and spectra of NGC 3191 as the host of the SN II PTF10bgl, as well as results from the MPA-JHU analysis of SDSS DR7 galaxies, finding it to be a massive spiral galaxy with a stellar mass of $M_* \approx 5 \times 10^{10} M_\odot$ and a central oxygen abundance of $12 + \log[\text{O}/\text{H}] \approx 8.9$ on the Tremonti et al. (2004) strong-line scale. This implies a metallicity of $Z \approx 1.6 Z_\odot$, assuming a solar oxygen abundance of $12 + \log[\text{O}/\text{H}] = 8.69$ from Asplund et al. (2009). Nicholl et al. (2017) reported properties of the host NGC 3191 based on an archival data

analysis, and their results were in agreement with those reported in Kelly & Kirshner (2012).

The SDSS spectrum analyzed by Kelly & Kirshner (2012) is centered on the core of the galaxy and offset by ~ 3 kpc ($5''$) from the position of the SN. In order to estimate the metallicity at the location of the SN, we used the FAST spectrograph on the 60 inch Tillinghast telescope at F. L. Whipple Observatory with a relatively wide slit to obtain a late-time optical spectrum (on 2017 June 21.2) spanning a wider region of the galaxy and including the SN. After correcting for Milky Way reddening, we find line fluxes of $f(\text{H}\alpha) = 9.96 \times 10^{-14} \text{ erg s}^{-1} \text{ cm}^{-2}$ and $f([\text{N II}]) = 3.32 \times 10^{-14} \text{ erg s}^{-1} \text{ cm}^{-2}$, implying an abundance of $12 + \log[\text{O}/\text{H}] = 9.0$ using the Nagao et al. (2006) oxygen abundance calibration for the $[\text{N II}]/\text{H}\alpha$ ratio. This abundance estimator is on the same scale as Tremonti et al. (2004).

In contrast, most SLSN-I hosts are found in metal-poor dwarf galaxies (Lunnan et al. 2014). P16 analyzed 32 SLSNe-I discovered by the Palomar Transient Factory (PTF; Law et al. 2009) and concluded that they are almost exclusively found in metal-poor and star-forming dwarf galaxies having $M_* \lesssim 2 \times 10^9 M_\odot$ and $12 + \log[\text{O}/\text{H}] < 8.4$. Similar analyses by Schulze et al. (2018) of 53 SLSNe-I at $z < 1$ and C17 of SLSNe-I at $z < 0.3$ concluded that SLSNe-I are strongly suppressed for stellar masses $\gtrsim 10^{10} M_\odot$, and that SLSN-I production has a metallicity “cutoff” at $\sim 0.5 Z_\odot$.

As a check on the results of Kelly & Kirshner (2012) for NGC 3191, we carried out an independent analysis of its spectral energy distribution (SED). We fit the SDSS and GALEX photometry of the host using FAST (Kriek et al. 2009) with the Bruzual & Charlot (2003) stellar population synthesis models, a Chabrier (2003) initial mass function (IMF), an exponential star formation history, and solar ($Z = 0.02$) metallicity. We find a slightly lower stellar mass of $\log(M_*/M_\odot) = 10.21^{+0.17}_{-0.06}$, owing to different assumptions about the IMF, and a specific star

⁴⁰ <http://csp2.lco.cl/not/>

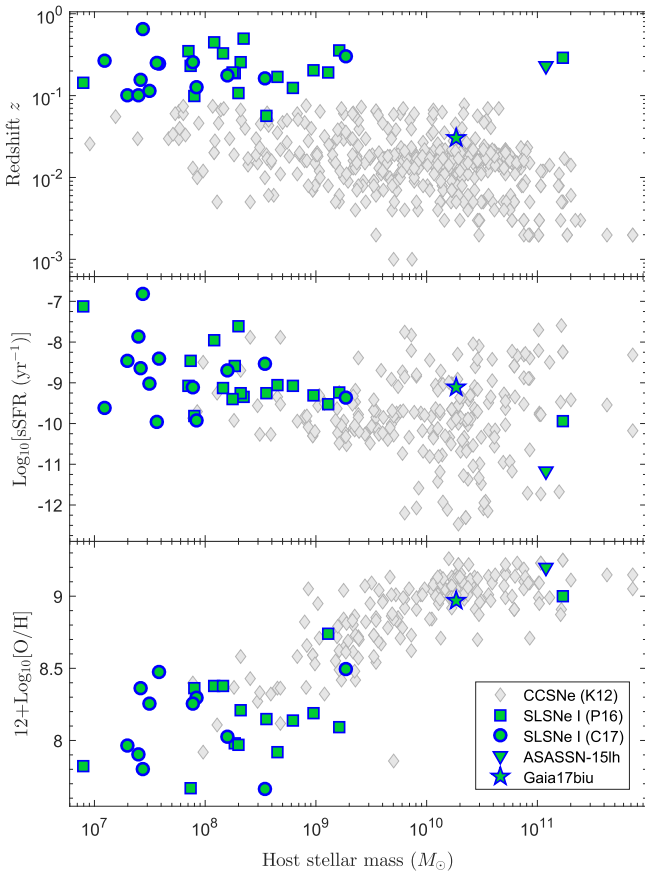


Figure 2. Distribution of SLSNe-I in redshift (top), specific star formation rate (middle), and metallicity (bottom) as a function of stellar mass. Gaia17biu is shown as a green star. The green squares and circles display a comparison SLSNe-I sample drawn from the PTF (P16) and the $z < 0.3$ sample (C17) augmented by the host of ASASSN-15lh (green triangle; Dong et al. 2016; Margutti et al. 2017b). Some ccSN host-galaxy properties from Kelly & Kirshner (2012) (K12) are also shown with gray symbols.

formation rate of $\log(\text{sSFR}) = -9.11^{+0.90}_{-0.38}$. This is for an age of $\log(\text{age}) = 8.55^{+0.57}_{-0.20}$ and a star formation timescale of $\log(\tau) = 8.1^{+0.9}_{-0.1}$.

In Figure 2, we compare the redshift, mass, star formation rate, and oxygen abundance of NGC 3191 with SLSNe-I hosts from the PTF sample by (P16) and the $z < 0.3$ sample by (C17) augmented by the host of ASASSN-15lh ($z = 0.2326$; Dong et al. 2016; Margutti et al. 2017b). The oxygen abundance values of C17 are converted from the Pettini & Pagel (2004) metallicity scale to the Tremonti et al. (2004) scale using the transformation given by Kewley & Ellison (2008), so that all the metallicity estimates are on a common scale. Our methodology for galaxy parameter estimates follows closely those adopted by P16 and C17, so that the comparisons with these samples are made on the same stellar mass (using the Chabrier 2003 IMF) and oxygen abundance (using the calibration of Nagao et al. 2006) scales. The sample of hosts from P16 and C17 has stellar masses up to $10^9 M_{\odot}$. However, there are few additional SLSNe-I hosts having stellar masses up to $10^{10} M_{\odot}$ (see, e.g., Lunnan et al. 2014; Schulze et al. 2018), but those are not included in the comparison sample (Figure 2) due to the lack of oxygen abundance information. The host galaxy of Gaia17biu, NGC 3191, has a higher mass and metallicity than the comparison SLSNe-I host sample, although its properties are typical of the general population of star-forming

galaxies (e.g., Yates et al. 2012) and the hosts of core-collapse SNe (ccSNe; e.g., Prieto et al. 2008; Kelly & Kirshner 2012; Stoll et al. 2013). The only SLSNe-I hosts similar to NGC 3191 in mass and metallicity are the host of PTF10uhf in the PTF sample and ASASSN-15lh (Dong et al. 2016; Margutti et al. 2017b). Since the redshift of PTF10uhf is typical of the other SLSNe-I in the PTF sample, the rarity of additional higher-mass and higher-metallicity hosts drives the conclusion that low metallicity is favored for producing SLSNe-I. However, Gaia17biu is found at a record-breaking low redshift, and the relative deficiency of low-redshift ($z < 0.05$) SLSNe-I with dwarf hosts implies that any suppression of SLSNe-I production in metal-rich and massive hosts is likely weaker than previously thought.

The location of Gaia17biu has an offset of $5''16$ (3.47 kpc) from the center of NGC 3191, which, after normalizing by the half-light radius (r band), implies an offset of 0.67. This is somewhat on the lower side as compared to the distribution found for SLSNe-I hosts (e.g., Lunnan et al. 2015; C17) having a median-normalized offset of ~ 1 . Interestingly, SLSNe with massive hosts in these samples tend to have larger offsets, which is opposite to that observed in the case of Gaia17biu.

4. Optical Observations

4.1. Data Collection and Reduction

In addition to the ASAS-SN V -band observations, multiband optical photometric observations were obtained with the Apogee Alta U230 camera at Post Observatory SRO (CA, USA) and the Apogee Alta U47 at Post Observatory Mayhill (NM, USA) with 0.6 m telescopes at both locations, the 0.5 m Dedicated MONitor of EXotransits and Transients (DEMONEXT; Villanueva et al. 2016) and the 0.5 m Iowa Robotic Telescope (both at the Winer Observatory, AZ, USA), the IO:O imager on the 2.0 m Liverpool Telescope (LT) at La Palma, ALFOSC and NOTCam on the 2.5 m NOT at La Palma, the Las Cumbres Observatory 1.0 m telescope network (Brown et al. 2013), the 1.0 m Nickel telescope at Lick Observatory (CA, USA), the 1.0 m telescope at Weihai Observatory of Shandong University (China) (Hu et al. 2014), the 2.0 m Ritchey-Chretien telescope at Bulgarian National Astronomical Observatory (Rozhen, Bulgaria), and the Meade 10 inch LX-200 Schmidt-Cassegrain Telescope at Antelope Hills Observatory (CO, USA).

We triggered observations with *Swift* (Gehrels et al. 2004) lasting from 2017 June 2 to July 4 (PI: S. Dong; *Swift* Target IDs 10150 and 10154) to obtain near-UV (NUV) observations with the Ultraviolet Optical Telescope (UVOT; Roming et al. 2005). Except for the ASAS-SN difference-imaging analysis pipeline, point-spread function (PSF) photometry was done with the DoPHOT (Schechter et al. 1993) package for the optical and near-infrared (NIR) data. Optical photometric data were calibrated using APASS⁴¹ standards for the Johnson BV filters and the Sloan (AB magnitude system) gri filters, and the JHK NIR data were calibrated using 2MASS (Skrutskie et al. 2006) standards. The *Swift*/UVOT photometry was measured with UVOTSOURCE task in the Heasoft package using $5''$ apertures and placed in the Vega magnitude system, adopting the revised zero points and sensitivity from Breeveld et al. (2011). The reduced photometry is reported in Table 1.

⁴¹ <https://www.aavso.org/apass>

Optical spectroscopic observations were obtained using ALFOSC on NOT, the Kast Dual Channel Spectrograph mounted on the 3 m Shane telescope at Lick Observatory (CA, USA; Miller & Stone 1993), the B&C spectrograph mounted on the 1.2 m Galileo Telescope and the AFOSC spectrograph on the 1.8 m Copernico telescope in Asiago (Italy), the FAST spectrograph (Fabricant et al. 1998) mounted on the 60" Tillinghast telescope at F. L. Whipple Observatory (AZ, USA), and the SPRAT spectrograph mounted on the 2.0 m Liverpool telescope in La Palma. Most spectra were taken at or near the parallactic angle (Filippenko 1982) to minimize differential slit losses caused by atmospheric dispersion. The log of optical spectroscopic observations is given in Table 3.

The ALFOSC and AFOSC data were reduced using FOSCGUL.⁴² The FAST spectra were reduced with the standard pipeline system using IRAF⁴³ scripts developed for FAST and Massey standards (Massey et al. 1988; Massey & Gronwall 1990) for spectrophotometric calibration. SPRAT spectra were reduced and flux-calibrated using the LT pipeline (Barnsley et al. 2012; Piascik et al. 2014). Kast data were reduced following standard techniques for CCD processing and spectrum extraction (Silverman et al. 2012) utilizing IRAF routines and custom Python and IDL codes.⁴⁴ Low-order polynomial fits to comparison-lamp spectra were used to calibrate the wavelength scale, and small adjustments derived from night-sky lines in the target frames were applied. Observations of appropriate spectrophotometric standard stars were used to flux-calibrate the spectra. Spectra from other instruments were reduced and calibrated using standard procedures. Telluric corrections were applied to remove strong atmospheric absorption bands. For some spectra where appropriate telluric standards were not available, we manually removed the region strongly affected by telluric features. We also obtained spectra of Gaia17biu in the NIR at -3 days using the Aerospace Corporation's Visible and Near-Infrared Imaging Spectrograph (VNIRIS) on the Lick Observatory 3 m Shane reflector, near maximum light (-0.5 days) using the Spex medium-resolution spectrograph ($0.7\text{--}5.3\ \mu\text{m}$; Rayner et al. 2003) on the NASA Infrared Telescope Facility (IRTF), and at -0.8 days with NOTCam. The spectra are reduced and calibrated using standard methods.

Three epochs of spectropolarimetry were obtained using the polarimetry mode of Lick/Kast on 2017 June 21 (-1 day), June 27 ($+5$ day), and July 1 ($+9$ day). On June 21, the source was observed just after 12° twilight and over a moderately high airmass range of $1.58\text{--}1.89$, as it was setting. The June 26 and July 1 data were obtained progressively deeper into twilight, as the sky position of the setting source became increasingly unfavorable. Polarization spectra were measured at each of four waveplate angles (0° , 45° , 22.5° , and 67.5°), with three exposures obtained at each angle to remove cosmic rays via median combination. The individual exposures were 270, 200, and 140 s for the June 21, 26, and July 1 observations, respectively, for total integration times of 3240, 2400, and 1680 s over all waveplate angles. Low-polarization standard stars were observed to calibrate the instrumental position-angle

curve with respect to wavelength and to confirm that the instrumental polarization was negligible. High-polarization standard stars were observed to calibrate the polarization position angle on the sky, θ . All of the spectropolarimetric reductions and calculations follow the methodology described by Mauerhan et al. (2014, 2015), and the polarimetric parameters are defined in the same manner. We refer the reader to those works for more detailed information on the observations and reductions.

4.2. Photometric Evolution

In Figure 3, we show the full set of multiband light curves, where we adopt the peak⁴⁵ of the g -band light curve at $\text{JD } 2,457,926.3 \pm 0.7$ (2017 June 21.8) as our reference epoch throughout this paper.

After correcting for Galactic extinction and applying small K -corrections based on the optical spectroscopy, Gaia17biu peaked at $M_g = -20.97 \pm 0.05$ mag, which is close to the mean SLSN-I peak magnitude (De Cia et al. 2017; Lunnan et al. 2018). In Figure 4, we compare its g -band light curve to those of a number of other SLSNe-I, mainly from the sample of Nicholl et al. (2015b) and adding SN 2015bn (Nicholl et al. 2016) and Gaia16apd (Kangas et al. 2017).

Almost all well-observed SLSNe-I appear to show significant curvatures in their light curves near their peaks (see Figure 4). Some SLSNe-I (the most conspicuous example is SN 2015bn (Nicholl et al. 2016), but also LSQ14bdq and LSQ14mo) show sporadic undulations in their light curves. In contrast, the light-curve evolution of Gaia17biu from ~ -20 to ~ 20 days can be almost perfectly described by a linear rise followed by a linear decline in magnitude (shown as yellow dashed lines in Figure 4) with a rapid (few-day) turnaround at the peak. The linearity of the light curves implies that the SN luminosity is evolving exponentially in both the rise to the peak and decline from the peak. Such photometric evolution appears to be unprecedented among SLSNe-I. The rise time for Gaia17biu, characterized by the e -folding time $\tau_{g\text{-rise}} \approx 20$ days before the peak, is relatively fast. This is consistent with the general trend that the less-luminous SLSNe-I have faster rise times, as evident from Figure 4. Inserra & Smartt (2014) also noted a similar positive correlation, but between the decline timescale and the luminosity. However, Gaia17biu is one of the slowest-declining SLSNe-I despite having a lower luminosity. A few other SLSNe have also been found to not follow this correlation, most notably PS1-14bj (Lunnan et al. 2016), which has both long rise and decline timescales. We have insufficient observational coverage to directly measure one e -folding in flux in the decline of Gaia17biu. Nevertheless, following the almost perfect exponential flux decline as we see here, the e -folding decline time is estimated to be $\tau_{g\text{-decl.}} \approx 60$ days. Thus, Gaia17biu combines one of the fastest rise times with one of the slowest declines.

Nicholl & Smartt (2016) studied light curves of several SLSNe-I showing possible double peaks similar to LSQ14bdq (Nicholl et al. 2015a) and proposed that an early-time luminosity excess is ubiquitous in SLSNe-I. However, we do not see clear evidence for such an early, pre-peak bump in the smoothly evolving ASAS-SN V -band light curve of Gaia17biu. There is a possible dip with $V = 18.7 \pm 0.5$ mag at 2017 May

⁴² Developed by E. Cappellaro; <http://sngroup.oapd.inaf.it/foscgui.html>.

⁴³ IRAF is distributed by the National Optical Astronomy Observatory, which is operated by the Association of Universities for Research in Astronomy (AURA) under a cooperative agreement with the US National Science Foundation.

⁴⁴ <https://github.com/ishivvers/TheKastShiv>

⁴⁵ The peak was found by fitting a fourth-order polynomial to the flux values close to maximum brightness (± 15 days).

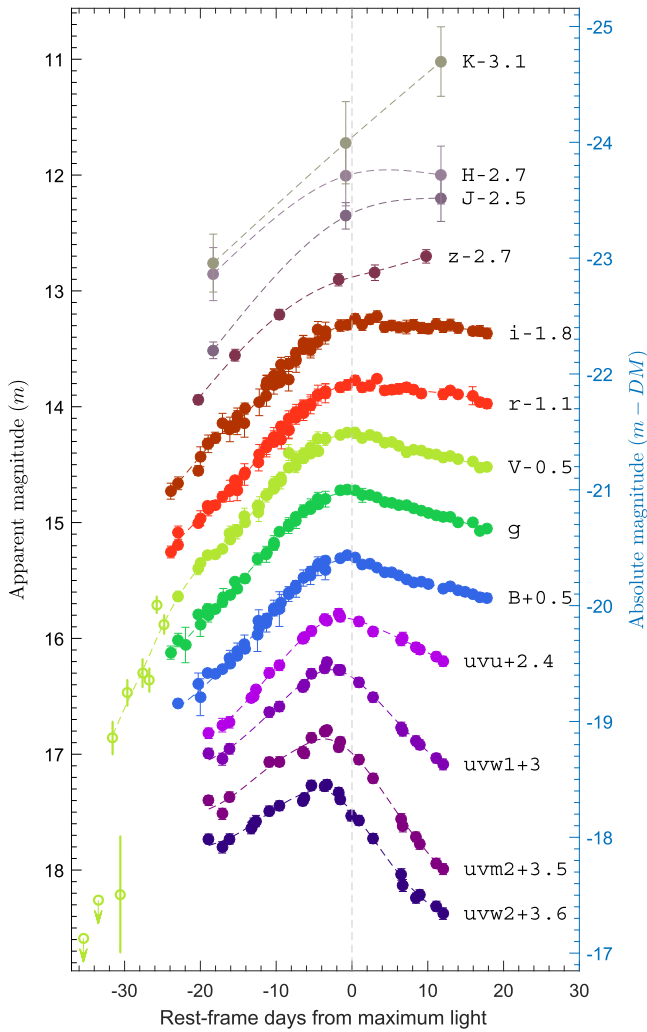


Figure 3. Johnson-Cousins BV , SDSS $griz$, *Swift*-UVOT NUV (Vega magnitude), and JHK light curves of Gaia17biu. The light curves are shifted vertically for clarity. The reference epoch is set by the g -band maximum (JD 2,457,926.3). Low-order splines are shown to connect the data for visual clarity. The light green open circles are V -band detections from ASAS-SN, and the ones with downward arrows represent ASAS-SN upper limits. The data used to create this figure are available.

21.30 (phase = -30.6 days), as compared with $V = 17.4 \pm 0.1$ mag 1 day earlier (-31.6 day) and $V = 17.0 \pm 0.1$ mag 1 day later (-29.6 days), but the evidence for a dip has low statistical significance, and the implied timescale (~ 1 day) is considerably shorter than the early bump seen in LSQ14bdq (Nicholl et al. 2015a). Overall, there is no evidence in our data for any significant departure (including precursor “bumps” as reported in Nicholl & Smartt 2016 or “undulations” as seen in the light curves of SN 2015bn by Nicholl et al. 2016) from a smooth light-curve evolution.

Only a handful of low-redshift SLSNe-I have wavelength coverage with good cadence like that for Gaia17biu. The first panel of Figure 5 shows the evolution of the *Swift* NUV ($uvw2$ band at 2080 \AA) to optical (SDSS r band at 6254 \AA) color of Gaia17biu and three other SLSNe-I where such data are available (Gaia16apd, Kangas et al. 2017; SN 2015bn, Nicholl et al. 2016; ASASSN-15lh, Dong et al. 2016). Due to the lack of NUV spectroscopic observations for (most phases of) these

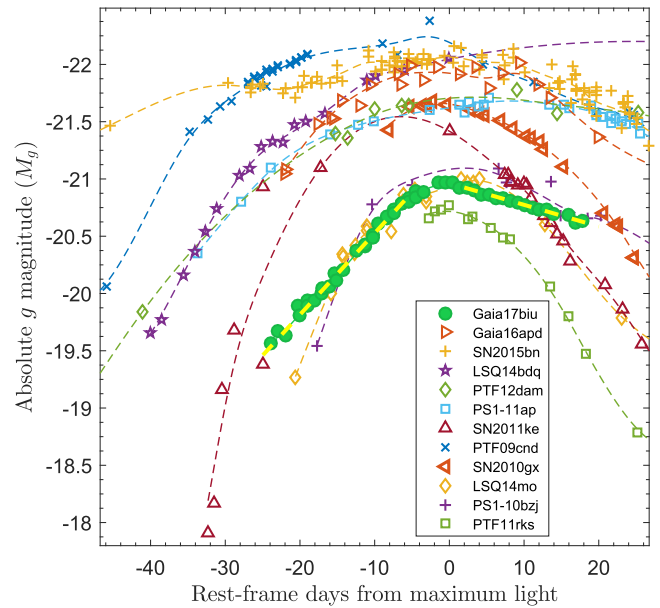


Figure 4. Absolute g -band light curve of Gaia17biu as compared to other SLSNe-I. The sample is mainly based on that in Nicholl et al. (2015b), with the addition of two recently discovered low- z SLSNe-I, SN 2015bn and Gaia16apd. The full sample includes Gaia16apd (Kangas et al. 2017), SN 2015bn (Nicholl et al. 2016), LSQ14bdq (Nicholl et al. 2015a), PTF12dam (Nicholl et al. 2013), PS1-11ap (McCrum et al. 2014), SN 2011ke (Inserra et al. 2013), PTF09cnd (Quimby et al. 2011), SN 2010gx (Pastorello et al. 2010), LSQ14mo (Chen et al. 2017a), PS1-10bzj (Lunnan et al. 2013), and PTF11rks (Inserra et al. 2013). A pair of yellow dashed lines are shown on the rising and declining parts of Gaia17biu to illustrate their remarkable linearity.

comparison SNe, we assumed blackbody SEDs to compute and apply K -corrections based on effective temperatures. Gaia17biu closely follows the color evolution of Gaia16apd, which has one of the bluest UV-to-optical colors among SLSNe-I (Kangas et al. 2017; Yan et al. 2017). Yan et al. (2017) attributed this blue color to reduced line blanketing due to both the newly synthesized metals in the ejecta and the likely subsolar progenitor as deduced from its dwarf host. The latter reasoning is difficult to apply to Gaia17biu owing to its relatively high host-galaxy metallicity (see Section 3).

We also fit the NUV through z -band photometry of Gaia17biu with blackbody SEDs.⁴⁶ The second, third, and fourth panels of Figure 5 show the resulting rest-frame estimates for the evolution of the effective temperature, blackbody radius, and bolometric luminosity. The estimated parameters are given in Table 2. The blackbody models fit the SEDs well. Gaia17biu evolves in temperature like Gaia16apd but has a significantly smaller photosphere and hence luminosity. Gaia16apd evolves in radius like ASASSN-15lh but is significantly cooler and hence less luminous. SN 2015bn is cooler but larger in radius than Gaia17biu, Gaia16apd, and ASASSN-15lh, leading to a luminosity intermediate to those of the other three sources. While the sample of SLSNe-I with good multiwavelength photometry is limited, the population appears to show a considerable diversity in size and temperature to accompany the range of luminosities. We note that near -19 days, there is an apparent short decline lasting for

⁴⁶ The SED is redshifted to the observed frame prior to filter-response convolution and fitting.

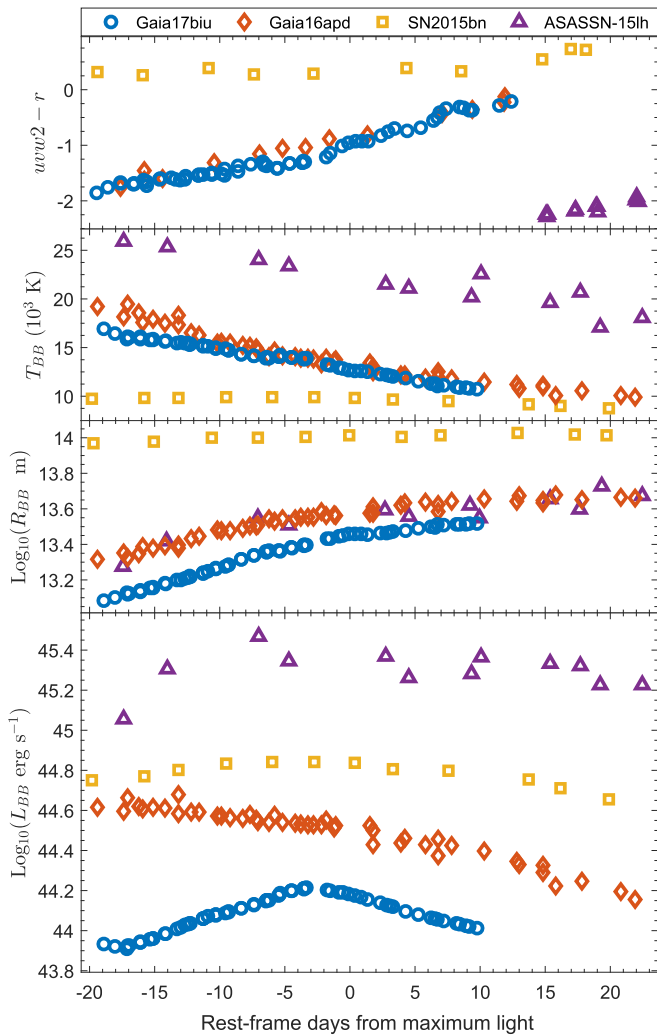


Figure 5. Evolution of NUV ($uvw2$) to optical (r) colors, blackbody temperature, radius, and luminosity of Gaia17biu as compared to the handful of SLSNe-I having good NUV and optical coverage.

only 2 days. However, we do not consider it to be a significant indication for a “bump,” as this originated from only one epoch (-18.9 days) of data points in the UVOT NUV bands (see Figure 3). Even though we have significant optical observations before -19 days, we do not find any such indication of a bump.

4.3. Spectroscopy

The spectroscopic evolution of Gaia17biu is shown in Figure 6. As already noted in Section 2, it exhibits the strong W-shaped O II absorption lines at rest-frame ~ 4100 and ~ 4400 Å that are characteristic of most known SLSNe-I. Our earliest spectra show these features at $\sim 20,000$ km s $^{-1}$ with broad, extended, and somewhat flat-bottomed shapes. As the velocities decrease with time, the line shapes become sharper and more similar to those exhibited by SN 2010gx (Pastorello et al. 2010; see the comparison in Figure 10). After reaching peak brightness, the O II features start to become weaker and are overtaken by other metallic lines.

To identify the spectral features in Gaia17biu, we model the spectra using SYNOW (Fisher et al. 1997, 1999; Branch et al. 2002), a parameterized spectrum synthesis code with an

underlying LTE continuum, assuming pure resonant scattering and radiative transfer is simplified using a Sobolev approximation. We selected the latest available spectra for modeling, as at this phase the spectral features are most prominent. The $+25.6$ day Kast spectrum is used with the missing portion near 5500 Å stitched with the $+26.2$ day AFOSC spectrum. In Figure 7, we show the best-fit model spectrum using a combination of O I, Fe II, Na I, S II, C II, Mg II, Si II, and Ca II atomic species. An exponential optical depth profile is found to be suitable for reproducing the observed line profiles. All the spectral features are formed at a single velocity of roughly $\approx 10,500 \pm 1000$ km s $^{-1}$, which further confirms our line identifications. In Figure 7, the ions labeled in black are used in SYNOW to synthesize the corresponding spectral feature in the model spectrum. The ions labeled in blue are identified based only on their velocity but have not been used to produce the corresponding model feature. These ions can also reproduce P Cygni profiles at the labeled location using the exact same velocity as other lines (i.e., $\approx 10,500$ km s $^{-1}$). However, at the same time, the given ion will also produce several additional sets of features (of relative strengths) in the model that are not present in the observed spectrum. The Sc II/S II features near 5500 Å are prominent examples of such an ambiguous identification. The model spectrum can produce these features using S II, as well as Sc II, at similar wavelengths and using the same velocity. However, increasing the strength of Sc II to match the target feature would also produce unmatched strong features near 4100 Å. On the other hand, if the progenitors of SLSNe are massive, the presence of Sc II is more likely than that of S II. The ambiguity of Sc II (and other features labeled in blue) can also be due to the unknown complexity of radiation transfer and non-LTE SED for Gaia17biu, which are beyond the simplified assumptions in SYNOW. We also modeled the $+13$ day spectrum to confirm the identification of C II features near 6400 and 7100 Å (as labeled in Figure 6).

At ~ 4450 Å, close to the longer-wavelength doublet component of the W-shaped O II feature, we find an apparent double absorption feature that is labeled as “A” in Figure 6. Such a feature has not previously been observed in SLSNe-I to our knowledge. It is most prominent in the ~ 5 day spectrum and still appears to be present but with a different shape in the ~ 10 day spectrum. The feature can be traced back to the earliest spectrum, where it is likely weakly blended with the longer-wavelength doublet component of the W-shaped feature, possibly (partly) contributing to its flat-bottomed profile. As the ejecta velocities decline, this feature becomes more clearly resolved.

A shallow feature is also visible in the early-time spectra near 5500 Å until the $\sim +5$ day spectrum. This feature is also visible in SN 2015bn and Gaia16apd and has been attributed to C III $\lambda 5690$. Another broad feature near 6300 Å is attributed to C II $\lambda 6580$ (Yan et al. 2017), which we also find in our SYNOW modeling of the later phase spectra. One prominent metallic line is Fe II $\lambda 5169$. This feature appeared at ~ -13 day with $\sim 10,000$ km s $^{-1}$ and remained until the last spectrum with little velocity evolution. Such a non-evolving Fe II line has also been observed in other SLSNe-I (e.g., Nicholl et al. 2015b; Kangas et al. 2017).

Apart from these features, the early-time spectra are mostly devoid of other prominent features, while at later phases, heavily blended metallic lines start to appear. Blends of a few Fe II, Na I D, and possible S II/Sc II multiplets near

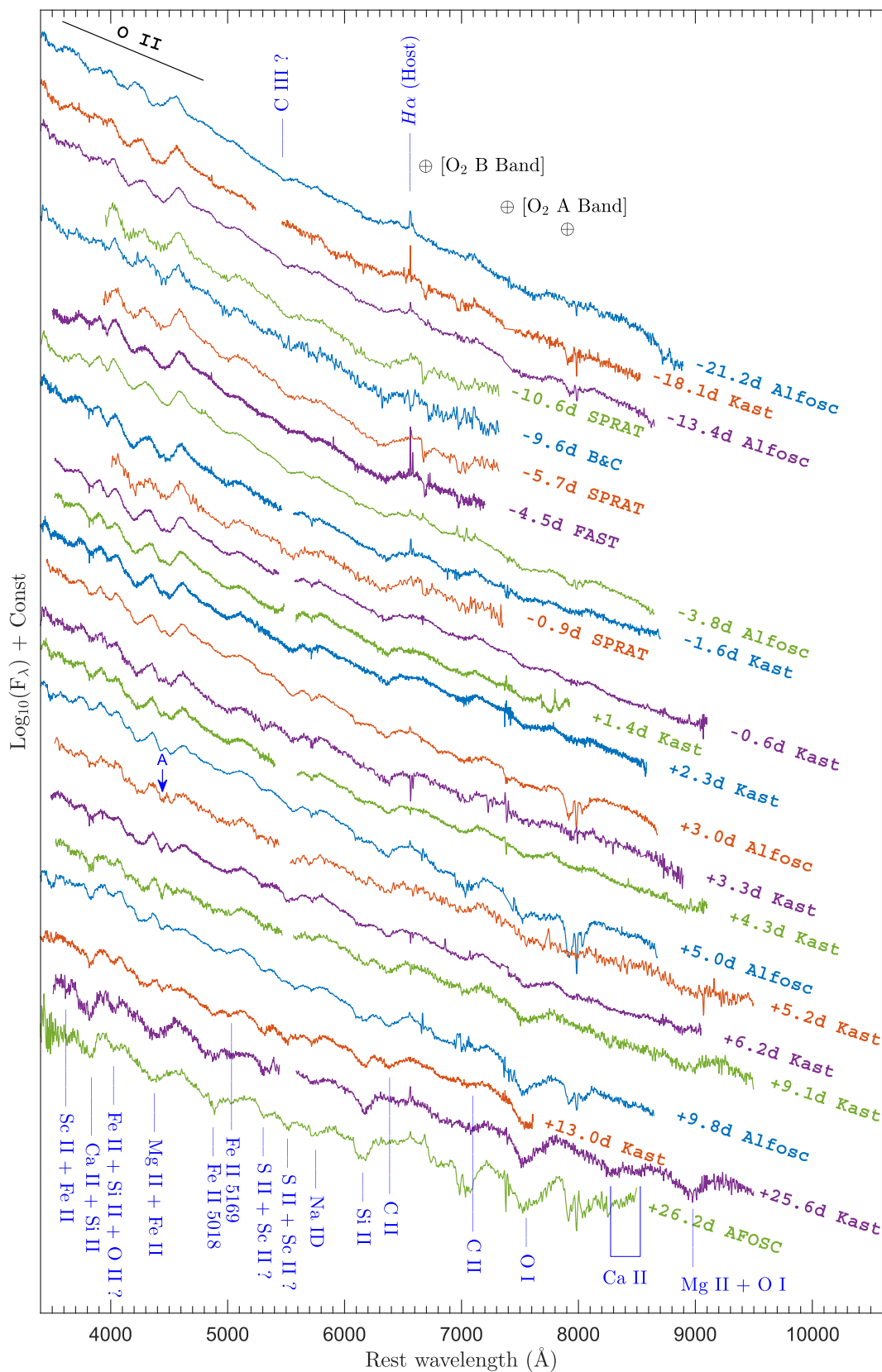


Figure 6. Rest-frame spectral evolution of Gaia17biu. The wavelength range for the features attributed to O II is indicated by the black line at the top. Other spectral features are marked by vertical blue lines. The arrow marked “A” indicates an unidentified spectral feature not previously detected in SLSNe-I (discussed in Section 4.2). Each spectrum is labeled by the instrument used and the rest-frame phase from maximum light. The data used to create this figure are available.

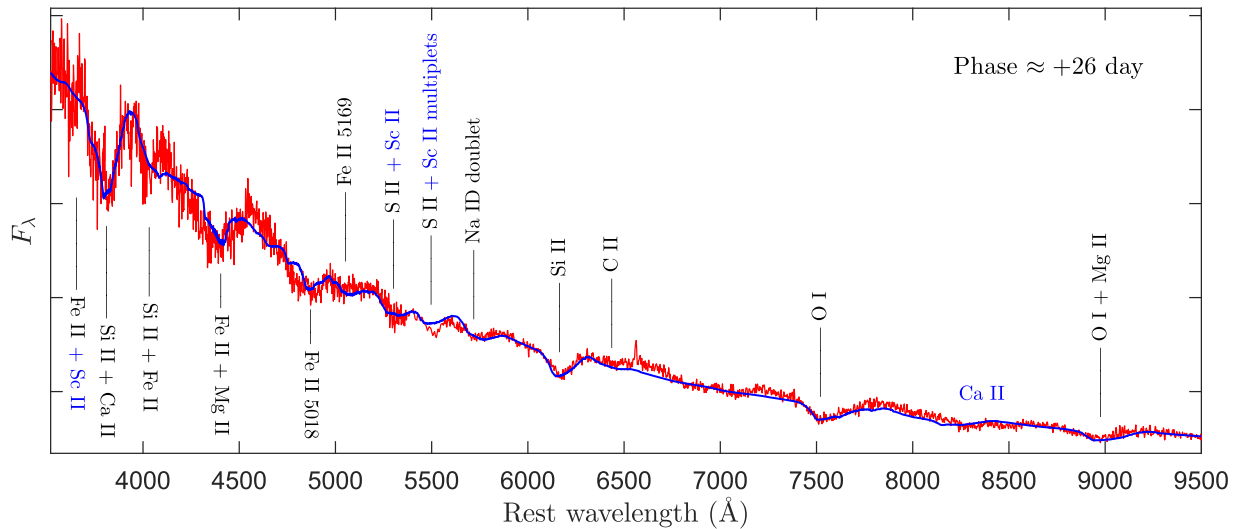


Figure 7. A SYNOW model spectrum (blue solid line) is generated to reproduce the observed $\approx +26$ day Gaia17biu spectrum (red solid line). The line velocity for all of the identified features is $\approx 10,500$ km s $^{-1}$. The ions labeled in black are used to synthesize the corresponding spectral features. The ions labeled in blue are not used in the model but are identified based on their wavelengths and assuming the same

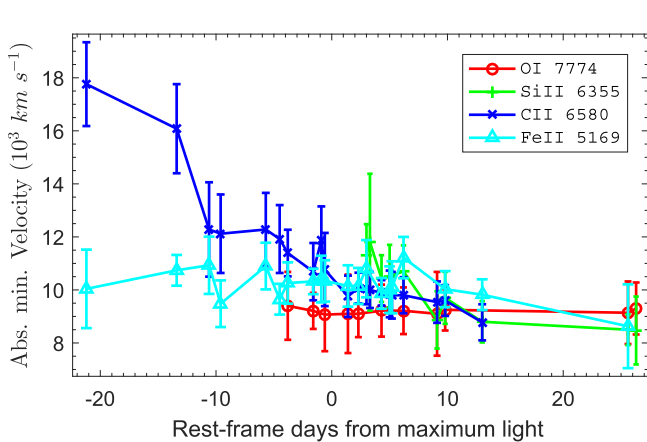


Figure 8. Line velocity evolution for Fe II $\lambda 5169$, Si II $\lambda 6355$, O I $\lambda 7774$, and C II $\lambda 6580$. The velocities are estimated from the absorption minima of the corresponding P Cygni profiles.

4900–5600 Å can be identified in the +13 day spectrum and become more prominent at later phases. Such a clear detection of these Fe II and S II/Sc II metallic lines in SLSNe is uncommon. In particular, the $\sim +26$ day spectrum shows a remarkable transition compared to the previous spectra: later spectra are dominated by numerous strong metal-rich features. At this phase, we see the emergence of the Ca II $\lambda\lambda 3969, 3750$ doublet, along with Fe II $\lambda 5018$; the Na I D $\lambda\lambda 5890, 5896$ doublet; and the Ca II $\lambda\lambda 8498, 8542, 8662$ NIR triplet. Other features that become significantly stronger than in previous spectra are Si II $\lambda 6355$, O I $\lambda 7774$, and Mg II near 9000 Å. This likely marks the start of the transition to the spectrum of a normal SN Ic, as seen in some other SLSNe-I (Pastorello et al. 2010).

Figure 8 shows the velocity evolution of the Fe II $\lambda 5169$, Si II $\lambda 6355$, O I $\lambda 7774$, and C II $\lambda 6580$ lines, estimated by measuring the absorption minima of the P Cygni profiles. These lines are well-identified and free from strong blending with neighboring lines in all of the spectra. The line velocities, particularly for Fe II and O I, remain almost constant with time. This is commonly observed in other SLSNe-I as well (e.g., Nicholl et al. 2015b, 2016; see also Figure 9). The

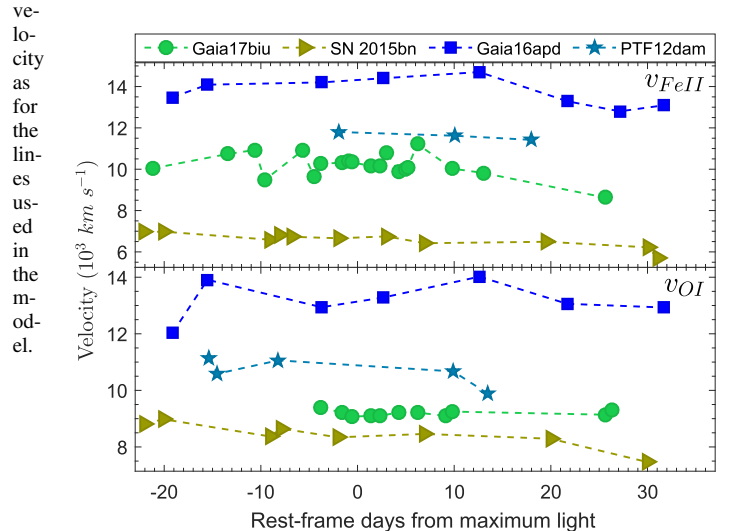


Figure 9. Fe II and O I $\lambda 7774$ line velocities of Gaia17biu as compared to SN 2015bn (Nicholl et al. 2016), Gaia16apd (Kangas et al. 2017), and PTF12dam (Nicholl et al. 2013). The Fe II velocities are measured using the $\lambda 5169$ line, except for SN 2015bn, where the $\lambda 4924$ line is used. In the case of PTF12dam, the Fe II $\lambda 5169$ velocities are presented in Nicholl et al. (2015b), while the O I velocities are measured from spectra (Nicholl et al. 2013).

constant velocity evolution may possibly indicate stratification of line-forming shells within a homologous expansion. On the other hand, the C II velocity shows a monotonic decline with time, which is consistent with a typical spherical SN model where deeper and slower-moving layers are exposed by a receding photosphere. In Figure 9, we compare the Fe II $\lambda 5169$ and O I $\lambda 7774$ velocity evolution with other well-observed SLSNe: SN 2015bn (Nicholl et al. 2016), Gaia16apd (Kangas et al. 2017), and PTF12dam (Nicholl et al. 2013). For SN 2015bn, the Fe II $\lambda 4924$ line velocity is used because the Fe II $\lambda 5169$ line profile appears to be contaminated by Fe III emission in the early phases. Gaia17biu and the comparison sample all show very little velocity evolution. The Fe II line velocity for Gaia17biu remains almost constant at $\sim 10,000$ km s $^{-1}$, which is very close to the median velocity of $10,500$ km s $^{-1}$ for the SLSN-I sample compiled by Nicholl et al. (2015b).

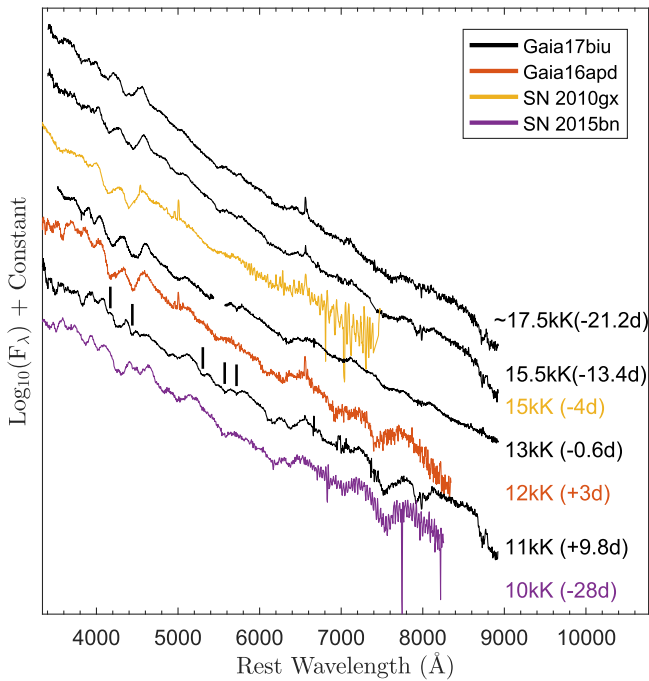


Figure 10. Rest-frame spectra of Gaia17biu as compared with spectra of the SLSNe-I SN 2010gx (Pastorello et al. 2010), SN 2015bn (Nicholl et al. 2016), and Gaia16apd (Kangas et al. 2017). Some weak line features that are not visible in the spectra of other SLSNe-I are marked with solid black lines on the day 10 spectrum. In addition to the name of the SN and the epoch of observation, each spectrum is labeled with the estimated blackbody temperature of the SN in units of $\text{kK} = 10^3 \text{ K}$.

Since Gaia17biu is the apparently brightest SLSN observed to date by a factor of nearly 10, it provided an unprecedented opportunity to obtain high-S/N spectra. In Figure 10, we have marked several additional broad or weak spectroscopic features that apparently have not been previously seen in any SLSN-I spectra, presumably because of their typically lower S/Ns. We also note that some of these features appear to be only visible for short periods of time, and possibly our high spectroscopic cadence has helped in capturing Gaia17biu during such transitions. These features could be blended metallic lines that become more visible as the line velocities decrease. A few of these features near 5400 \AA are likely associated with metallic lines such as Fe II and S II/Sc II, which become more prominent at later phases (see the ~ 25 day spectra; Figure 6).

In Figure 10, we compare the spectra of Gaia17biu to those of other SLSNe-I at three different phases representing the pre-, near-, and post-peak phases of evolution. We tried to match the Gaia17biu spectra to other SLSNe-I using a large number of existing SLSN-I spectra prepared by Liu et al. (2017) as SNID (Blondin & Tonry 2007) templates and available in WiseREP (Yaron & Gal-Yam 2012). In general, we found that spectra corresponding to epochs with comparable blackbody temperatures have the best similarity in spectral features, rather than spectra with comparable phases (relative to maximum light), as is usually done in such comparisons (e.g., Liu et al. 2017). This is illustrated in Figure 10, where we report the estimated temperature along with the epoch for each spectrum. A good example is that an ~ 10 day post-peak spectrum of Gaia17biu is best matched by

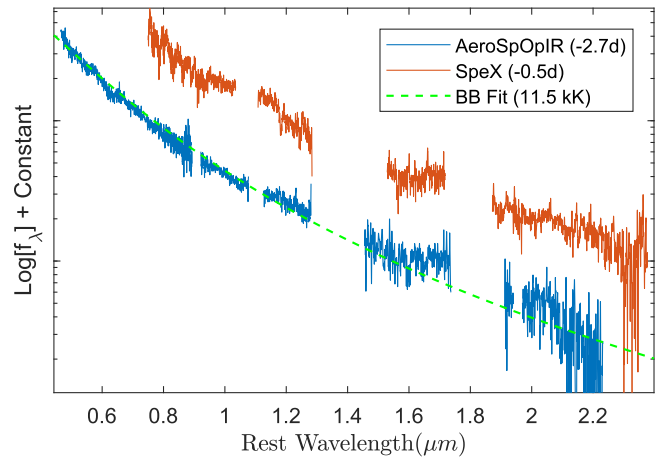


Figure 11. Infrared spectra at two epochs. No prominent features are detectable given the low S/N of these spectra. The continuum follows the blackbody SED, as shown with a dashed green line at a temperature of 11.5 kK. Strong telluric and unreliable regions in the spectra are masked out. The data used to create this figure are available.

a -28 day pre-peak spectrum of SN 2015bn, where both sources have estimated temperatures of $\sim 10,000 \text{ K}$.

SLSNe-I are sometimes divided into fast- and slow-decline populations based on the post-peak decline rates. Nicholl et al. (2016) argued that the spectra near peak show differences in several features for the two populations, and Kangas et al. (2017) showed that Gaia16apd appears to “bridge” the two populations in terms of its decline rate and spectra. The post-peak decline rate of Gaia17biu makes it a member of the slow-decline population, but its pre-peak spectra most closely resemble those of the prototypical fast-decline SLSN-I SN 2010gx, even while its post-peak spectra most closely resemble those of the slow-decline SLSN-I SN 2015bn. At peak, Gaia17biu is spectroscopically similar to Gaia16apd. This suggests that the light-curve decline rate is unlikely to be a useful indicator for describing the spectroscopic diversity of the SLSN-I population.

Figure 11 shows the NIR spectra obtained for Gaia17biu at -2.7 and -0.5 days. All NIR spectra are smooth, and we do not detect any significant features from either the SN or its host galaxy. He I $\lambda 10833$ is the most prominent feature detected in a few SLSNe-I (e.g., Gaia16apd, Yan et al. 2017; SN 2012li, Inserra et al. 2013). However, for Gaia17biu, we were unable to conclude anything about the presence of He I due to very strong telluric line contamination in that wavelength range. The SED from the optical through NIR wavelengths shows a continuum consistent with the Rayleigh–Jeans tail of a thermal blackbody.

4.4. Spectropolarimetry

The only other SLSN-I with spectropolarimetric observations is SN 2015bn, where Inserra et al. (2016) found a significant and increasing degree of polarization between -24 and $+27$ days. Their results indicated the presence of a consistent dominant axis at both epochs and a strong wavelength dependence of polarization. Broadband polarimetric observations are available for two SLSNe-I, 2015bn (Leloudas et al. 2017) and LSQ14mo (Leloudas et al. 2015a). Broadband polarimetry of SN 2015bn also showed increasing

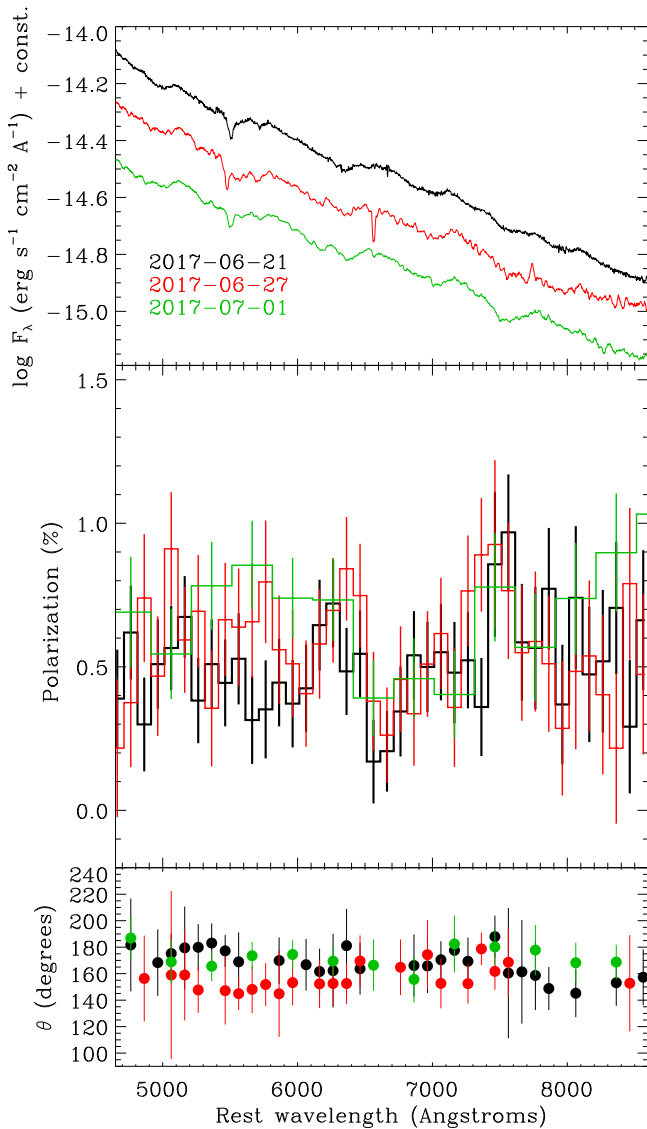


Figure 12. Three epochs of spectropolarimetry for Gaia17biu. Top panel: observed Kast spectra, color-coded for each epoch. Middle panel: polarization, given as the rotated Stokes q parameter (see Mauerhan et al. 2014). The June and July data have been binned by 100 and 300 Å, respectively. Bottom panel: position angle (θ) for the corresponding epochs, binned to 100 Å.

polarization until +46 days, while for LSQ14mo, the broadband polarization during -7 to +19 days suggested overall spherical symmetry.

Our spectropolarimetric results (see Figure 12) show that we have detected significant polarization in Gaia17biu. To determine whether this polarization is intrinsic to the SN, we must first address the possibility of interstellar polarization (ISP) induced by the dichroic absorption of SN light by interstellar dust grains aligned with the magnetic field of the interstellar medium. Fortunately, the ISP in the direction of Gaia17biu appears to be low ($E(B-V) \approx 0.0097 \pm 0.0005$ mag; see Section 1). According to Serkowski et al. (1975), the maximum expected polarization correlates with reddening by $P_{\text{ISP}} < 9 E(B-V)\%$, which implies $P_{\text{ISP}} < 0.09\%$ from the Milky Way in the direction of Gaia17biu. There are also polarimetric measurements in the literature of a

nearby F0 V star, HD 89536 ($0^\circ.58$ away from Gaia17biu), that lies at an estimated spectroscopic-parallax distance of ~ 193 pc, sufficiently distant to be useful as a probe of the intervening ISP. The cataloged optical polarization of HD 89536 is a null detection with $P < 0.025\%$ (Berdyugin et al. 2014). We thus do not expect significant Galactic ISP in the direction of Gaia17biu.

The ISP from the host galaxy is more difficult to ascertain, but the lack of significant Na I D absorption features at the rest wavelength of NGC 3191 suggests that the host absorption is likely to be less than the low Milky Way value. Furthermore, if the polarization were due to ISP, then we would expect a Serkowski functional form, whereby the polarization peaks near a wavelength of 5500 Å and drops off at longer wavelengths (Serkowski et al. 1975). Instead, the average polarization appears to be relatively flat with wavelength, which is more consistent with the effects of electron scattering. We are therefore inclined to interpret the polarized signal as intrinsic to the SN.

Under the reasonably justified assumption of unsubstantial ISP, it appears that significant intrinsic polarization in the continuum and possible modulations across line features have been detected in Gaia17biu. The “continuum polarization” (integrated over the wavelength range 7800–8700 Å, where the spectra appear to be devoid of line features) is $P_{\text{cont}} = 0.43\% \pm 0.09\%$ at $\theta = 161^\circ \pm 6^\circ$. Taken at face value, the electron-scattering models used by Hoflich (1991) would suggest that this level of polarization is consistent with an ellipsoidal shape on the sky having an axis ratio of ~ 0.9 . Modulations relative to the continuum appear as high as 0.4%–0.5%, particularly in the regions near 6300–6400 and 7300–7600 Å. The modulations could thus be associated with blueshifted absorption components of the possible C II $\lambda 6580$ and O I $\lambda 7774$ lines. The lack of strong deviations in θ across these features is consistent with global asphericity of the SN atmosphere and its line-forming region, as opposed to a clumpy or irregular line-forming region, which typically results in substantial position-angle changes (see, e.g., Mauerhan et al. 2015). Comparison of the June 21 and 27 data indicates no substantial change in the polarization characteristics between these epochs; slight shifts in polarization and θ at select wavelengths are near the limit of statistical significance. However, comparison of the June 21 and July 1 data shows a slight indication that the polarization has marginally increased around 5000–6000 Å, possibly associated with the Si II or C II lines. However, the bright night-sky emission lines in this region of the spectrum were particularly strong and rapidly changing, as the observations were performed in substantial twilight, and the polarization increase should be treated with caution.

5. Radio Observations

We observed the location of Gaia17biu at 1.5 GHz with the electronic Multi-Element Remotely-Linked Interferometer Network (e-MERLIN) from 2017 June 21 to 23 and with the Karl G. Jansky Very Large Array (VLA) on 2017 June 22 and 30. The e-MERLIN observations were made in two continuous runs with a bandwidth of 512 MHz (1254.6–1766.5 MHz), reduced to ~ 400 MHz after flagging, using the Knockin, Pickmere, Darnhall, and Cambridge stations, along with the Mark II (18:00 June 21 to 12:00 June 22) and Defford (15:00

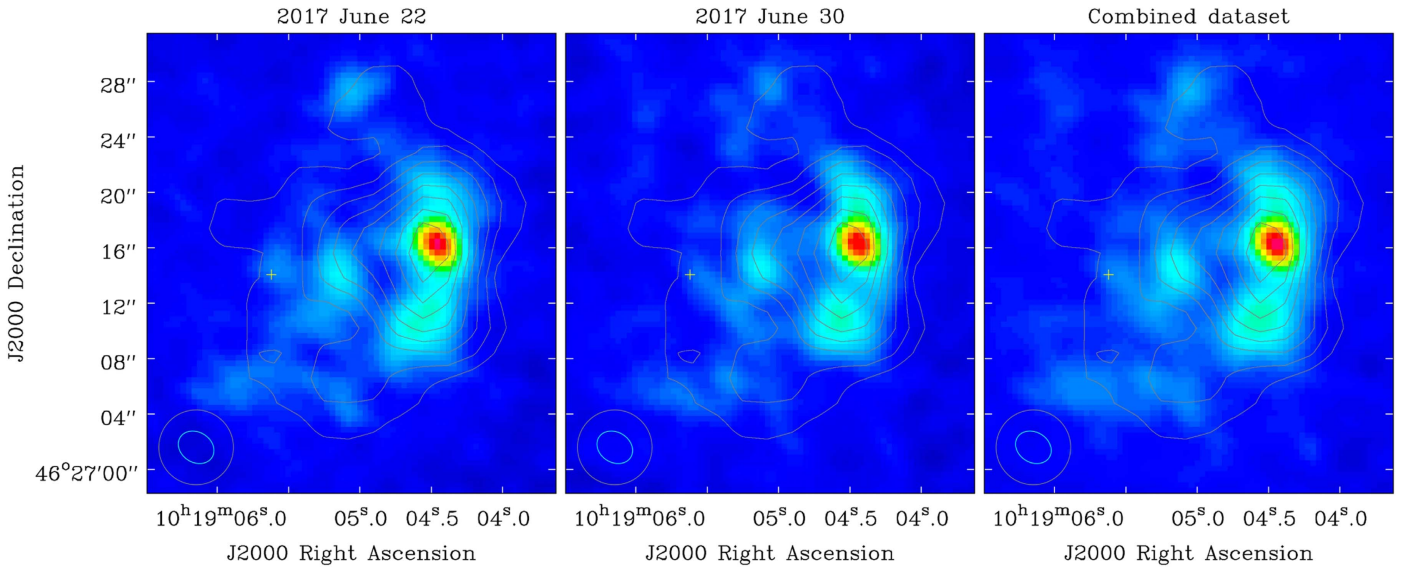


Figure 13. NGC 3191 10 GHz VLA maps from June 22 (left), June 30 (middle), and the combined data set (right) at a resolution of $2''.72 \times 2''.18$, P.A. = 58° . Overlaid in each map, we show the cutout from the Faint Images of the Radio Sky at Twenty-cm survey (FIRST; Becker et al. 1995) with a full width at half-maximum intensity (FWHM) of $5''.4 \times 5''.4$. The beams are shown in the lower left corner of each map; the white one corresponds to the recent VLA maps and the gray one to the FIRST image cutout. The position of Gaia17biu is indicated with a yellow cross.

June 22 to 11:00 June 23) stations. The data were reduced and analyzed with the National Radio Astronomy Observatory (NRAO) Astronomical Image Processing System (AIPS) following standard procedures. We used 3C 286 as a flux calibrator and OQ 208 as a bandpass calibrator. The phase reference source J1027+4803 (at a projected distance of $2''.11$ from the SN position) had a 1.5 GHz flux density of 147.6 mJy, which remained constant during the time of the observations. The resolution was 203×130 mas at P.A. = $-18^\circ 8'$. The extended emission of the host galaxy is resolved out in these observations, and we measure a root-mean-square (rms) noise level of $32 \mu\text{Jy beam}^{-1}$ at the SN position, corresponding to a 1.5 GHz luminosity limit of $<2 \times 10^{27} \text{ erg s}^{-1} \text{ Hz}^{-1}$ at a 3 σ level.

Gaia17biu was also observed at a central frequency of 10 GHz with the VLA on 2017 June 22 and 30. The data were reduced using Common Astronomy Software Applications package (CASA; McMullin et al. 2007) version 4.7.2 with some additional data flagging. The observations had a total bandwidth of 4 GHz with full polarization using 3C 286 as the flux and bandpass calibrator and J0958+4725 (at a projected distance of $3''.67$ from Gaia17biu) as the phase reference source. We achieved rms noise levels of 5.9 and $5.8 \mu\text{Jy beam}^{-1}$ for the June 22 and 30 epochs, respectively. As shown in Figure 13, using a common convolving beam ($2''.72 \times 2''.18$, P.A. = 58°) to ease comparisons between the epochs, the host galaxy is resolved and well detected. The brightest structure peaks at $\alpha(\text{J2000}) = 10^{\text{h}}19^{\text{m}}04^{\text{s}}.45$ ($\pm 0''.03$), $\delta(\text{J2000}) = 46^\circ 27' 16''.3$ ($\pm 0''.03$). This source is coincident with a strong star-forming region detected in the optical and an SDSS spectrum consistent with an H II region. The nucleus of the host at $\alpha(\text{J2000}) = 10^{\text{h}}19^{\text{m}}05^{\text{s}}.14$ ($\pm 0''.19$), $\delta(\text{J2000}) = 46^\circ 27' 14''.6$ ($\pm 0''.19$) is relatively fainter. While there is plenty of diffuse emission from the host at the position of the SN, we do not detect any point source at the position of the SN (Romero-Canizales

et al. 2017) and no evidence for variability between the two epochs. The estimated detection limits are $25.6 \mu\text{Jy beam}^{-1}$ and $28.7 \mu\text{Jy beam}^{-1}$ on June 22 and 30, respectively, with a combined limit of $23.3 \mu\text{Jy beam}^{-1}$ corresponding to 5.4×10^{26} units.

Radio observations are particularly important as a test for powering SLSNe-I with GRB-like central engines. Observations of SN 2015bn 238 days after maximum light placed an upper limit of $<2 \times 10^{28} \text{ erg s}^{-1} \text{ Hz}^{-1}$, ruling out its association with a typical long GRB and various off-axis geometries (Nicholl et al. 2016). However, owing to the late phase of the radio observations, they were not able to place meaningful constraints on an association with the low-luminosity GRBs (possibly not highly collimated) that dominate the local GRB rate.

In the case of Gaia17biu, we have the advantage of proximity (factor of 3.7 closer than SN 2015bn), allowing us to put a tighter upper limit on the radio luminosity of $<5.4 \times 10^{26} \text{ erg s}^{-1} \text{ Hz}^{-1}$ at 10 GHz. Furthermore, our radio observations were taken close to the optical peak, when the radio afterglow luminosity would also be expected to be near maximum for low-luminosity GRBs. Using the radio upper limit of Gaia17biu, we can rule out its association with low-luminosity GRBs across most of the observed luminosities. When low-luminosity GRBs have been observed in the radio (e.g., Galama et al. 1998; Soderberg et al. 2004, 2006; Margutti et al. 2013), their 8.5 GHz luminosities are generally 10^{28} – $10^{29} \text{ erg s}^{-1} \text{ Hz}^{-1}$ at phases similar to those when Gaia17biu was at $<5.4 \times 10^{26} \text{ erg s}^{-1} \text{ Hz}^{-1}$, with the exception of GRB 060218 at $\sim 10^{27} \text{ erg s}^{-1} \text{ Hz}^{-1}$. This appears to largely rule out an association of this SLSN-I with a GRB radio afterglow.

Comparing our radio upper limit around day 30 after explosion with typical radio fluxes of SNe Ibc (Soderberg et al. 2010), we find that Gaia17biu must have been a weaker source than most SNe Ibc. A normal SN Ibc with a spectrum

that peaks at 10 GHz around 30 days has a flux of $\sim 2 \times 10^{27} \text{ erg s}^{-1} \text{ Hz}^{-1}$, significantly higher than our upper limit of $5.4 \times 10^{26} \text{ erg s}^{-1} \text{ Hz}^{-1}$. However, judging from Soderberg et al. (2010), if the spectral peak at this epoch was below ~ 3 GHz, an SN Ibc would most likely go undetected in our data. Likewise, for a spectral peak above ~ 20 GHz at 30 days, synchrotron self-absorption would make a detection unlikely. Thus, our 10 GHz data cannot rule out that Gaia17biu could be an SN Ibc-like radio source, although it would be among the weakest in this class. For example, SNe 2003gk (Bietenholz et al. 2014) and 2014C (Margutti et al. 2017a) would both have been undetected at 30 days given our upper limits, despite these SNe being much brighter at later epochs.

The radio observations presented in this paper place stringent upper limits on the radio emission from this source, showing no evidence for strong interactions of the ejecta with the CSM at this point in its evolution. Further deep radio observations are required to determine if interaction between the ejecta and the CSM at later times may result in greater levels of radio emission due to relatively dense CSM.

6. X-Ray Observations

Swift also observed the field of Gaia17biu with its X-ray telescope (XRT; Burrows et al. 2005) for a total of 33,661 s. All observations were performed in photon-counting mode (PC mode; Hill et al. 2004) and processed in the standard way by running *xrtpipeline*. The resulting event files were then combined in *XSELECT* in order to obtain spectra, event files, and images. X-ray positions were determined by using the online XRT product tool at the University of Leicester website.⁴⁷ For the average X-ray spectrum, we created an auxiliary response file (arf) for each single observation using the task *xrtmkarf* and combined them into a single arf using the FTOOL task *addarf*. We used the XRT PC mode response file *swxpc0to12s6_20130101v014.rmf*. The spectral analysis was performed using XSPEC version 12.8.2 (Arnaud et al. 1985).

After coadding the data for the first two weeks of *Swift* observations, we noticed enhanced X-ray emission close to the optical position of Gaia17biu. This period had a total exposure time of 13 ks (Grupe et al. 2017a). We measured the position of this X-ray source to be $\alpha_{J2000} = 10^{\text{h}}19^{\text{m}}05^{\text{s}}77$, $\delta_{J2000} = +46^{\circ}27'14''.1$ with an uncertainty of $5''.1$. This position was $4''.6$ away from the optical counterpart of Gaia17biu and $7''.3$ from the center of NGC 3191, the host galaxy of Gaia17biu. Applying the Bayesian method described by Kraft et al. (1991), we obtained a count rate in the 0.3–10 keV energy range of $(9.5^{+3.2}_{-2.7} \times 10^{-4} \text{ counts s}^{-1})$, which corresponds to a flux in the 0.3–10 keV band of $4.1^{+1.6}_{-1.4} \times 10^{-14} \text{ erg s}^{-1} \text{ cm}^{-2}$. Assuming that this X-ray source is located at the distance of NGC 3191 ($D_L = 139$ Mpc), this corresponds to a luminosity of $10^{41} \text{ erg s}^{-1}$.

Although the X-ray position obtained over the first two weeks of *Swift* observations initially suggested that this X-ray source may well be the counterpart of Gaia17biu, adding more observations in the following weeks made this conclusion less convincing (Grupe et al. 2017b). Our new analysis included all available data obtained between 2017 June 2 and July 4. The X-ray spectrum of the X-ray source can be fitted by a single power-law model with the absorption column density fixed to the Galactic value ($N_{\text{H}} = 9.39 \times 10^{19} \text{ cm}^{-2}$; Kalberla

et al. 2005), a photon index $\Gamma = 1.88^{+0.51}_{-0.49}$, and a flux in the observed 0.3–10 keV band of $2.9^{+1.2}_{-0.6} \times 10^{-14} \text{ erg s}^{-1} \text{ cm}^{-2}$. The count rate obtained from these data is $9.0^{+1.9}_{-1.7} \times 10^{-4} \text{ counts s}^{-1}$. There is no evidence for any variability of the X-ray source. The source position in this 34 ks observation is $\alpha_{J2000} = 10^{\text{h}}19^{\text{m}}04^{\text{s}}96$, $\delta_{J2000} = +46^{\circ}27'15''.8$ with an uncertainty of $6''.4$. This position is $7''.0$ away from the optical position of Gaia17biu and $1''.7$ from the position of NGC 3191. This new position suggests that the X-ray emission is likely associated with the starburst region in the center of NGC 3191 and not coming from Gaia17biu.

We also obtained a 3σ upper limit at the optical position of the SN in the 0.3–10 keV range. We extracted source counts in a circular region with a radius of 2 pixels (equivalent to $4''.7$) centered on the optical position of Gaia17biu. The background was subtracted from an annulus with an inner radius of $3''$ and an outer radius of $10''$. Without PSF correction, we obtained a 3σ upper limit of $3.4 \times 10^{-3} \text{ counts s}^{-1}$, applying the Bayesian method by Kraft et al. (1991). Assuming the same spectral model as above, this corresponds to a flux limit in the 0.3–10 keV band of $1.1 \times 10^{-13} \text{ ergs s}^{-1} \text{ cm}^{-2}$, which, assuming the luminosity distance of NGC 3191, converts to a luminosity limit of $2.5 \times 10^{41} \text{ ergs s}^{-1}$. Due to the broad PSF of the *Swift* XRT, we caution that this limit may be weakened by strong contamination from the nearby star-forming region. A secure X-ray constraint at the 0.3–10 keV band around bolometric maximum could potentially test whether there are circumstellar interactions (e.g., Dwarkadas & Gruszko 2012).

7. Summary and Discussion

In summary, we identify Gaia17biu as the the lowest-redshift SLSN-I to date, exploding in a massive and metal-rich host galaxy that is typical of ccSNe but atypical of most known SLSNe-I. Previously, it was suggested that SLSN-I production might be strongly suppressed at high metallicities (e.g., Schulze et al. 2018), and the purported requirement for a metal-poor environment was seen as evidence supporting the birth of a fast-spinning magnetar as the central engine for SLSNe-I (e.g., P16). But the relatively high volume rate implied by the close distance of Gaia17biu suggests that any metallicity effect on the SLSN-I production rate is weaker than presently believed.

The curious fact that the two all-sky surveys for bright transients, ASAS-SN and *Gaia*, have both found SLSNe-I in massive, higher-metallicity galaxies demands explanation. It is difficult to explain as a selection effect in ASAS-SN or *Gaia*, since almost every observational selection effect in an untargeted transient survey favors higher survey efficiencies in less-luminous galaxies. A selection effect against non-dwarf galaxies in higher-redshift surveys seems more likely. For example, the discovery rate of tidal disruption events relative to SNe Ia (Holoien et al. 2016) and the radial distribution of SNe relative to the centers of galaxies in ASAS-SN (Holoien et al. 2017b) clearly show that amateurs and most professional surveys have been strongly biased against identifying transients close ($\sim \text{kpc}$) to the central regions of luminous galaxies where both ASASSN-15lh and Gaia17biu were discovered. For example, the median offset of Type Ia SNe in PTF is about 5 kpc (Lunnan et al. 2017), as compared to a median of 2.6 kpc in ASAS-SN (Holoien et al. 2017a) and the 3 kpc offset of Gaia17biu. This

⁴⁷ http://www.swift.ac.uk/user_objects

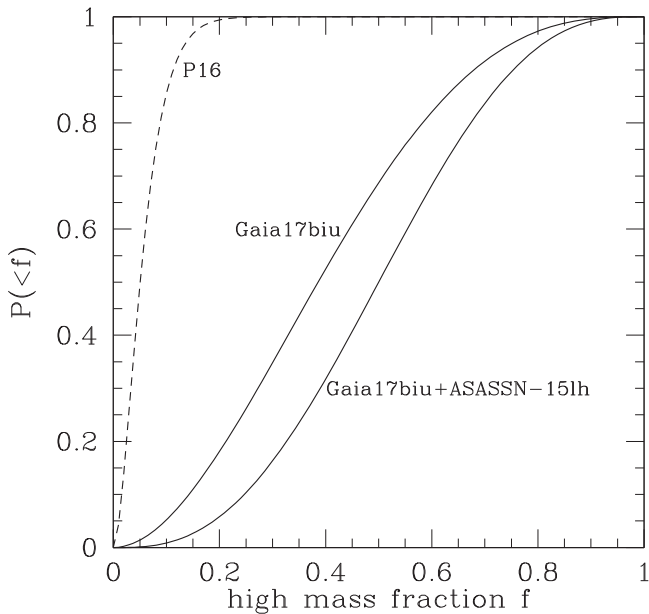


Figure 14. Integral probability distribution for the fraction of high-mass hosts of SLSNe-I. The dashed line shows the probability distribution of the **P16** sample, while the solid lines show the probability distribution for the *Gaia*/ASAS-SN sample, with and without including ASASSN-15lh.

incompleteness is likely a combination of the additional systematic problems in detecting transients in the central regions of luminous galaxies and a human bias against making expensive spectroscopic observations of candidate transients in regions with high false-positive rates.

We can roughly quantify the problem by assuming that the host stellar mass distribution from **P16** is representative and that the surveys differ only in their effective survey volumes due to the differences in photometric depth. Under these assumptions, the SLSN-I host mass and metallicity distributions in *Gaia* (or ASAS-SN) should be the same as those in PTF (**P16**). *Gaia* found two SLSNe-I, *Gaia17biu* and *Gaia16apd* (Kangas et al. 2017), where the latter is in a low-mass host. The ASAS-SN sample also includes two: SN 2015bn, which was discovered by PS1 (Huber et al. 2015) but recovered by ASAS-SN, and ASASSN-15lh (Dong et al. 2016). SN 2015bn is in a low-mass host, while ASASSN-15lh is in a high-mass host. We carry out our calculations both with and without ASASSN-15lh, since its identification as an SLSN-I is debated (Dong et al. 2016; Leloudas et al. 2016; Godoy-Rivera et al. 2017). The **P16** sample contains 32 SLSNe-I, one of which is in a high-mass host. The probability for the fraction f in high-mass hosts ($M_* \gtrsim 10^{10} M_\odot$) is simply the binomial distribution $P(f) \propto f(1-f)^{31}$, and we show the resulting integral probability distribution for f in Figure 14. The median estimate is $f = 0.050$ with a 90% confidence region of $0.011 < f < 0.14$. The *Gaia* and ASAS-SN low-redshift surveys have either $P(f) \propto f(1-f)^2$ without ASASSN-15lh or $f^2(1-f)^2$ if it is included. The integral distributions for these two cases are also shown in Figure 14, and we see that there is very little overlap. The medians for the low-redshift samples are $f = 0.39$ ($0.093 < f < 0.75$) without ASASSN-15lh and $f = 0.50$ ($0.19 < f < 0.81$) with ASASSN-15lh. Alternatively, we can average the probabilities of finding one (two) or more SLSNe-I in high-mass galaxies in the *Gaia*/ASAS-SN samples over the

probability of f implied by the **P16** sample, to find that there is only a 16% (2.5%) probability of such a result. These are not low enough likelihoods to be definitive; but, combined with the evidence that the higher-redshift surveys are biased against events as close to galactic centers as *Gaia17biu* and ASASSN-15lh, there is certainly a strong suggestion that the prevalence of SLSNe-I in high-mass galaxies is being underestimated. If we ignore the question of incompleteness, simply combining the low-redshift samples with **P16** raises the median to $f = 0.074$ (0.098) with a 90% confidence range of $0.023 < f < 0.16$ ($0.038 < f < 0.20$) excluding (including) ASASSN-15lh.

The proximity and high apparent brightness of *Gaia17biu* allowed us to carry out intensive and detailed follow-up observations during its early phases across a wide range of wavelengths. Its peak luminosity of $M_g \simeq -21$ mag is typical of known SLSN-I luminosity distribution (De Cia et al. 2017; Lunnan et al. 2018), and we find that its fast rise time is consistent with an empirical correlation between optical luminosity and rise time for well-observed SLSNe-I. We see no evidence for an early “bump” or undulations, as seen in several other SLSNe-I. Both its rise to the peak and decline from the peak follow strikingly simple exponential forms with a rapid reversal at the peak, and these features may help to distinguish theoretical models of powering mechanisms (e.g., Chatzopoulos et al. 2013).

While *Gaia17biu* is a slowly declining SLSN-I, its spectroscopic resemblance to both the fast- and slow-declining subclasses at different phases suggests that such a division may not be a useful description of the spectroscopic diversity of SLSNe-I. Our unprecedented high-S/N spectra also reveal several new features in SLSNe-I, potentially shedding new light on the chemical composition of the ejecta. We also identified new and subtle spectral features that are short-lived, and these detections were possible due to high-cadence and high-S/N spectroscopic observations. Apart from the extraordinarily linear rising and declining light curve, the photometric and spectroscopic features are broadly similar to those of other well-observed SLSNe-I. Given the very limited number of well-observed SLSNe, the uniquely identified features in *Gaia17biu* may not be characterized as unusual; rather, this possibly adds to the diversity of SLSNe-I.

In addition, we obtained spectropolarimetric observations, rare for a SLSN-I, showing that the ejecta are consistent with a global departure from spherical symmetry, the true extent of which is dependent on the uncertain viewing angle. Our uniquely tight constraint on its radio luminosity largely rules out an association of *Gaia17biu* with the GRB mechanism across the known luminosity function of radio afterglows.

The explosion model and energy supply mechanism for SLSNe-I are not known. Some proposed models include the spindown of highly magnetized, fast-rotating neutron stars (Bodenheimer & Ostriker 1974; Kasen & Bildsten 2010; Woosley 2010) or quark stars (Dai et al. 2016), pair-instability explosions (Barkat et al. 1967), and ejecta interactions with CSM (e.g., Blinnikov & Sorokina 2010; Sorokina et al. 2016). Thanks to its proximity, *Gaia17biu* is likely observable to very late evolution phases. Combined with the early-time data presented here, such late-time observations, especially the nebular-phase spectra, can help test theoretical models and clarify the chemical composition and ejecta structure. Also, late-time radio observations of *Gaia17biu* will be able to place strong constraints on possible associations with off-axis GRBs (e.g., Levinson et al. 2002).

Table 1
Photometry of Gaia17biu

UT Date	JD—2,457,000	Phase ^a (days)	<i>B</i> (mag)	<i>g</i> (mag)	<i>V</i> (mag)	<i>r</i> (mag)	<i>i</i> (mag)	Telescope ^b /Inst.
2017 May 16.29	889.79	-35.43	>19.090	AS
2017 May 18.31	891.81	-33.47	>18.760	AS
2017 May 20.26	893.76	-31.58	17.360 ± 0.140	AS
2017 May 21.30	894.80	-30.56	18.710 ± 0.500	AS
2017 May 22.26	895.76	-29.63	16.970 ± 0.110	AS
2017 May 24.33	897.83	-27.63	16.800 ± 0.120	AS
2017 May 25.25	898.75	-26.73	16.860 ± 0.100	AS
2017 May 26.25	899.75	-25.76	16.210 ± 0.070	AS
2017 May 27.28	900.78	-24.77	16.380 ± 0.080	AS
2017 May 28.16	901.66	-23.91	...	16.123 ± 0.057	...	16.354 ± 0.051	16.529 ± 0.069	Io
2017 May 29.16	902.66	-22.94	16.060 ± 0.034	...	16.136 ± 0.043	16.296 ± 0.035	16.461 ± 0.055	LCO
2017 May 29.18	902.68	-22.92	...	16.014 ± 0.058	...	16.187 ± 0.057	...	Io
2017 May 30.16	903.66	-21.97	...	16.057 ± 0.153	Io
2017 May 31.90	905.40	-20.29	15.895 ± 0.096	15.796 ± 0.028	15.899 ± 0.051	16.103 ± 0.023	16.350 ± 0.041	LT
2017 Jun 01.18	905.68	-20.01	16.008 ± 0.159	15.881 ± 0.102	15.849 ± 0.031	16.063 ± 0.065	16.232 ± 0.086	DN, Io, PO
2017 Jun 02.20	906.70	-19.02	15.800 ± 0.029	15.745 ± 0.043	15.780 ± 0.030	15.958 ± 0.041	16.119 ± 0.046	PO
2017 Jun 02.25	906.75	-18.97	...	15.797 ± 0.062	...	15.983 ± 0.059	16.120 ± 0.076	Io
2017 Jun 03.20	907.70	-18.05	15.806 ± 0.031	15.748 ± 0.024	15.775 ± 0.023	15.947 ± 0.037	16.067 ± 0.047	PO
2017 Jun 04.20	908.70	-17.08	15.766 ± 0.031	15.685 ± 0.045	15.724 ± 0.025	15.879 ± 0.045	15.944 ± 0.087	PO
2017 Jun 04.31	908.81	-16.98	...	15.645 ± 0.076	Io
2017 Jun 05.20	909.70	-16.11	15.673 ± 0.070	...	15.592 ± 0.061	15.826 ± 0.091	15.996 ± 0.106	DN
2017 Jun 05.21	909.71	-16.10	15.715 ± 0.027	15.626 ± 0.036	15.644 ± 0.029	15.818 ± 0.038	15.969 ± 0.044	PO
2017 Jun 05.94	910.44	-15.39	...	15.510 ± 0.030	15.569 ± 0.052	15.731 ± 0.024	15.975 ± 0.037	LT
2017 Jun 06.20	910.70	-15.14	15.610 ± 0.070	...	15.582 ± 0.059	15.821 ± 0.090	15.926 ± 0.115	DN
2017 Jun 06.22	910.72	-15.12	15.652 ± 0.029	15.573 ± 0.032	15.565 ± 0.031	15.756 ± 0.049	15.884 ± 0.050	PO
2017 Jun 07.19	911.69	-14.18	15.549 ± 0.078	...	15.447 ± 0.071	15.685 ± 0.093	15.940 ± 0.123	DN
2017 Jun 07.22	911.72	-14.15	15.587 ± 0.033	15.483 ± 0.038	15.495 ± 0.027	15.666 ± 0.029	15.816 ± 0.048	PO
2017 Jun 08.96	913.46	-12.47	15.471 ± 0.142	15.314 ± 0.052	15.359 ± 0.053	LT
2017 Jun 09.13	913.63	-12.30	15.347 ± 0.094	...	15.413 ± 0.078	15.576 ± 0.078	...	LCO
2017 Jun 09.20	913.70	-12.23	15.409 ± 0.072	...	15.354 ± 0.077	15.515 ± 0.089	15.762 ± 0.115	DN
2017 Jun 10.17	914.67	-11.29	...	15.274 ± 0.069	...	15.450 ± 0.062	15.616 ± 0.086	Io
2017 Jun 10.18	914.68	-11.28	15.366 ± 0.079	...	15.265 ± 0.058	15.450 ± 0.083	15.708 ± 0.088	DN
2017 Jun 10.20	914.70	-11.26	15.326 ± 0.026	15.262 ± 0.043	15.259 ± 0.035	15.430 ± 0.055	15.586 ± 0.059	PO
2017 Jun 11.17	915.67	-10.32	15.202 ± 0.042	15.394 ± 0.038	15.528 ± 0.056	LCO
2017 Jun 11.18	915.68	-10.31	15.238 ± 0.068	...	15.158 ± 0.056	15.361 ± 0.081	15.610 ± 0.081	DN
2017 Jun 11.20	915.70	-10.29	...	15.176 ± 0.063	...	15.361 ± 0.053	15.543 ± 0.066	Io
2017 Jun 11.20	915.70	-10.29	15.262 ± 0.026	15.196 ± 0.036	15.211 ± 0.039	15.407 ± 0.039	15.558 ± 0.048	PO
2017 Jun 11.90	916.40	-9.61	15.247 ± 0.150	15.076 ± 0.025	15.141 ± 0.050	15.356 ± 0.031	15.589 ± 0.032	LT
2017 Jun 12.17	916.67	-9.35	15.140 ± 0.070	15.270 ± 0.040	15.439 ± 0.065	PO
2017 Jun 12.20	916.70	-9.32	15.192 ± 0.072	...	15.117 ± 0.053	15.386 ± 0.078	15.525 ± 0.087	DN
2017 Jun 13.19	917.69	-8.36	...	15.034 ± 0.060	...	15.306 ± 0.065	15.431 ± 0.065	Io
2017 Jun 13.19	917.69	-8.36	15.117 ± 0.064	...	14.895 ± 0.069	15.298 ± 0.079	15.567 ± 0.097	DN
2017 Jun 13.20	917.70	-8.35	15.105 ± 0.029	15.015 ± 0.057	15.029 ± 0.037	15.204 ± 0.069	15.427 ± 0.044	PO
2017 Jun 14.20	918.70	-7.38	15.042 ± 0.026	14.951 ± 0.037	15.012 ± 0.057	15.147 ± 0.044	15.338 ± 0.046	PO
2017 Jun 14.20	918.70	-7.38	...	14.987 ± 0.064	...	15.195 ± 0.056	15.390 ± 0.067	Io
2017 Jun 14.20	918.70	-7.37	15.073 ± 0.072	...	14.944 ± 0.060	15.154 ± 0.074	15.406 ± 0.097	DN
2017 Jun 15.18	919.68	-6.43	...	14.902 ± 0.055	...	15.096 ± 0.055	15.247 ± 0.063	Io
2017 Jun 15.18	919.68	-6.43	14.979 ± 0.070	...	14.903 ± 0.048	15.117 ± 0.068	15.260 ± 0.074	DN
2017 Jun 15.21	919.71	-6.40	14.974 ± 0.026	14.900 ± 0.042	14.945 ± 0.044	15.152 ± 0.067	15.301 ± 0.044	PO
2017 Jun 16.18	920.68	-5.46	...	14.855 ± 0.059	...	15.073 ± 0.058	15.287 ± 0.074	Io
2017 Jun 16.18	920.68	-5.46	14.957 ± 0.078	...	14.848 ± 0.055	15.079 ± 0.082	15.312 ± 0.067	DN
2017 Jun 16.22	920.72	-5.42	14.925 ± 0.027	14.882 ± 0.028	14.902 ± 0.026	15.086 ± 0.040	15.262 ± 0.054	PO
2017 Jun 17.17	921.67	-4.50	...	14.796 ± 0.057	...	14.999 ± 0.052	15.242 ± 0.061	Io
2017 Jun 17.18	921.68	-4.49	14.877 ± 0.081	...	14.776 ± 0.059	15.001 ± 0.087	15.131 ± 0.067	DN
2017 Jun 17.22	921.72	-4.45	14.855 ± 0.028	14.845 ± 0.031	14.884 ± 0.033	PO
2017 Jun 18.17	922.67	-3.53	14.830 ± 0.039	...	14.777 ± 0.030	PO
2017 Jun 18.18	922.68	-3.52	14.909 ± 0.085	...	14.778 ± 0.056	14.984 ± 0.082	15.188 ± 0.071	DN
2017 Jun 18.20	922.70	-3.49	...	14.798 ± 0.068	...	14.963 ± 0.061	15.150 ± 0.080	Io
2017 Jun 20.20	924.70	-1.56	14.805 ± 0.027	14.720 ± 0.034	14.746 ± 0.039	14.934 ± 0.040	15.099 ± 0.050	PO
2017 Jun 21.19	925.69	-0.60	14.680 ± 0.070	...	14.770 ± 0.030	Ni
2017 Jun 21.22	925.72	-0.57	14.780 ± 0.028	14.714 ± 0.031	14.726 ± 0.024	14.911 ± 0.045	15.094 ± 0.042	PO
2017 Jun 22.22	926.72	0.40	14.799 ± 0.027	14.719 ± 0.032	14.726 ± 0.048	14.873 ± 0.042	15.041 ± 0.044	PO
2017 Jun 23.22	927.72	1.37	14.865 ± 0.026	14.765 ± 0.060	14.770 ± 0.040	14.934 ± 0.040	15.095 ± 0.046	PO
2017 Jun 24.19	928.69	2.31	14.840 ± 0.150	...	14.760 ± 0.040	Ni
2017 Jun 24.21	928.71	2.34	14.858 ± 0.026	14.763 ± 0.032	14.743 ± 0.025	14.917 ± 0.046	15.044 ± 0.043	PO
2017 Jun 25.22	929.72	3.31	14.888 ± 0.028	14.785 ± 0.031	14.761 ± 0.031	14.856 ± 0.019	15.022 ± 0.050	PO
2017 Jun 26.21	930.71	4.28	14.928 ± 0.030	14.825 ± 0.030	14.813 ± 0.037	14.960 ± 0.037	15.110 ± 0.046	PO
2017 Jun 27.22	931.72	5.26	14.929 ± 0.028	14.828 ± 0.030	14.806 ± 0.029	14.955 ± 0.040	15.098 ± 0.044	PO
2017 Jun 28.21	932.71	6.22	14.959 ± 0.026	14.853 ± 0.029	14.839 ± 0.038	14.945 ± 0.045	15.116 ± 0.046	PO

Table 1
(Continued)

UT Date	JD—2,457,000	Phase ^a (days)	<i>B</i> (mag)	<i>g</i> (mag)	<i>V</i> (mag)	<i>r</i> (mag)	<i>i</i> (mag)	Telescope ^b /Inst.
2017 Jun 29.21	933.71	7.19	14.987 ± 0.026	14.853 ± 0.033	14.893 ± 0.043	14.934 ± 0.040	15.112 ± 0.059	PO
2017 Jun 30.21	934.71	8.16	15.015 ± 0.030	14.875 ± 0.033	14.868 ± 0.030	14.955 ± 0.039	15.090 ± 0.043	PO
2017 Jul 01.21	935.71	9.13	15.011 ± 0.026	14.895 ± 0.026	14.880 ± 0.027	14.984 ± 0.038	15.120 ± 0.048	PO
2017 Jul 02.21	936.71	10.10	15.030 ± 0.032	14.919 ± 0.030	14.905 ± 0.030	...	15.126 ± 0.044	PO
2017 Jul 03.21	937.71	11.07	...	14.936 ± 0.027	14.913 ± 0.030	...	15.084 ± 0.044	PO
2017 Jul 04.21	938.71	12.04	15.071 ± 0.030	14.951 ± 0.035	14.938 ± 0.038	14.992 ± 0.046	15.112 ± 0.047	PO
2017 Jul 05.21	939.71	13.01	15.051 ± 0.032	14.953 ± 0.025	14.926 ± 0.030	14.961 ± 0.027	15.095 ± 0.051	PO
2017 Jul 06.21	940.71	13.98	15.083 ± 0.031	14.995 ± 0.030	14.950 ± 0.036	14.994 ± 0.028	15.120 ± 0.045	PO
2017 Jul 07.21	941.71	14.95	15.099 ± 0.036	PO
2017 Jul 08.20	942.70	15.91	15.118 ± 0.025	15.000 ± 0.020	14.974 ± 0.029	15.005 ± 0.078	15.150 ± 0.035	PO
2017 Jul 09.20	943.70	16.88	15.142 ± 0.036	15.069 ± 0.018	15.025 ± 0.041	15.059 ± 0.036	15.145 ± 0.046	PO
2017 Jul 10.20	944.70	17.85	15.149 ± 0.035	15.052 ± 0.028	15.022 ± 0.031	15.075 ± 0.039	15.167 ± 0.046	PO
UT Date	JD 2457000+	Phase ^a (days)	<i>z</i> (mag)	<i>J</i> (mag)	<i>H</i> (mag)	<i>K</i> (mag)	Telescope ^b /Inst.	
2017 May 31.90	905.40	-20.29	16.641 ± 0.041	LT	
2017 Jun 02.94	907.44	-18.30	...	16.013 ± 0.072	15.555 ± 0.229	15.860 ± 0.250	NC	
2017 Jun 05.94	910.44	-15.39	16.255 ± 0.051	LT	
2017 Jun 11.90	916.40	-9.61	15.903 ± 0.044	LT	
2017 Jun 19.92	924.42	-1.83	15.604 ± 0.053	AF	
2017 Jun 20.96	925.46	-0.82	...	14.852 ± 0.114	14.705 ± 0.261	14.821 ± 0.355	NC	
2017 Jun 24.93	929.43	3.03	15.543 ± 0.067	AF	
2017 Jul 01.89	936.39	9.79	15.402 ± 0.058	AF	
2017 Jul 03.90	938.40	11.74	...	14.700 ± 0.200	14.700 ± 0.250	14.120 ± 0.300	NC	
UT Date	JD 2457000+	Phase ^a (days)	<i>uvw2</i> (mag)	<i>uvm2</i> (mag)	<i>uvw1</i> (mag)	<i>uvu</i> (mag)	Telescope ^b /Inst.	
2017 Jun 02.32	906.82	-18.90	14.131 ± 0.042	13.900 ± 0.042	13.991 ± 0.043	14.419 ± 0.045	UVOT	
2017 Jun 04.15	908.65	-17.12	14.204 ± 0.049	14.015 ± 0.048	14.043 ± 0.052	14.349 ± 0.059	UVOT	
2017 Jun 05.18	909.68	-16.13	14.131 ± 0.044	13.867 ± 0.042	13.954 ± 0.045	14.325 ± 0.049	UVOT	
2017 Jun 08.08	912.58	-13.32	14.037 ± 0.050	14.114 ± 0.033	UVOT	
2017 Jun 08.41	912.91	-13.00	13.999 ± 0.048	14.102 ± 0.033	UVOT	
2017 Jun 08.75	913.25	-12.67	13.977 ± 0.049	14.039 ± 0.033	UVOT	
2017 Jun 10.53	915.03	-10.94	13.889 ± 0.042	13.568 ± 0.041	13.639 ± 0.042	13.896 ± 0.042	UVOT	
2017 Jun 11.96	916.46	-9.56	13.845 ± 0.042	13.564 ± 0.042	13.588 ± 0.044	13.834 ± 0.044	UVOT	
2017 Jun 15.11	919.61	-6.49	13.802 ± 0.042	13.479 ± 0.042	13.419 ± 0.042	13.604 ± 0.042	UVOT	
2017 Jun 15.38	919.88	-6.24	13.778 ± 0.043	13.492 ± 0.042	13.401 ± 0.043	13.590 ± 0.043	UVOT	
2017 Jun 16.28	920.78	-5.36	13.667 ± 0.042	13.356 ± 0.041	13.303 ± 0.042	13.537 ± 0.043	UVOT	
2017 Jun 18.13	922.63	-3.56	13.677 ± 0.042	13.306 ± 0.042	13.256 ± 0.042	13.432 ± 0.043	UVOT	
2017 Jun 18.36	922.86	-3.34	13.662 ± 0.042	13.294 ± 0.041	13.207 ± 0.042	13.444 ± 0.041	UVOT	
2017 Jun 20.03	924.53	-1.72	13.732 ± 0.044	13.437 ± 0.042	13.272 ± 0.044	13.386 ± 0.044	UVOT	
2017 Jun 20.33	924.83	-1.43	13.788 ± 0.042	13.393 ± 0.041	13.274 ± 0.042	13.415 ± 0.041	UVOT	
2017 Jun 21.66	926.16	-0.14	13.930 ± 0.046	UVOT	
2017 Jun 22.71	927.21	0.88	13.970 ± 0.042	13.545 ± 0.041	13.379 ± 0.041	13.456 ± 0.039	UVOT	
2017 Jun 24.71	929.21	2.82	14.128 ± 0.043	13.706 ± 0.041	13.509 ± 0.042	13.543 ± 0.040	UVOT	
2017 Jun 28.53	933.03	6.52	14.438 ± 0.050	14.059 ± 0.046	13.771 ± 0.048	13.617 ± 0.046	UVOT	
2017 Jun 28.73	933.23	6.72	14.533 ± 0.052	14.123 ± 0.048	13.795 ± 0.048	13.594 ± 0.047	UVOT	
2017 Jun 30.52	935.02	8.45	14.642 ± 0.044	14.214 ± 0.042	13.884 ± 0.042	13.674 ± 0.038	UVOT	
2017 Jun 30.98	935.48	8.91	14.615 ± 0.045	14.278 ± 0.043	13.917 ± 0.043	13.699 ± 0.039	UVOT	
2017 Jul 03.38	937.88	11.23	14.711 ± 0.042	14.440 ± 0.042	14.034 ± 0.041	13.755 ± 0.037	UVOT	
2017 Jul 04.14	938.64	11.97	14.776 ± 0.050	14.492 ± 0.047	14.088 ± 0.047	13.797 ± 0.043	UVOT	

Note.

The abbreviations of telescope/instrument used are as follows: AS—ASAS-SN; Io—0.5 m Iowa Robotic telescope; LCO—Las Cumbres Observatory 1 m telescope network; LT—2 m Liverpool Telescope; DN—0.5 m DEMONEXT telescope; PO—0.6 m telescopes of Post Observatory; Ni—1 m Nickel telescope; NC—NotCAM IR imager on 2.0 m NOT telescope; AF—ALFOSC mounted on 2.0 m NOT telescope; UVOT—Ultraviolet Optical Telescope onboard *Swift* satellite. Data observed within 5 hr are represented under a single-epoch observation.

Table 2
Best-fit Blackbody Parameters

Phase ^a (days)	Temperature T_{BB} (10^3 K)	Radius R_{BB} (10^{12} m)	Luminosity L_{BB} (10^{44} erg s ⁻¹)
-18.90	16.90 ± 0.35	12.15 ± 0.52	0.86 ± 0.10
-18.05	16.45 ± 0.33	12.65 ± 0.51	0.83 ± 0.10
-17.12	15.83 ± 0.41	13.47 ± 0.73	0.81 ± 0.12
-17.08	16.12 ± 0.37	13.21 ± 0.64	0.84 ± 0.11
-16.98	16.04 ± 0.38	13.36 ± 0.68	0.84 ± 0.12
-16.13	16.08 ± 0.31	13.62 ± 0.56	0.88 ± 0.10
-16.11	15.87 ± 0.34	13.89 ± 0.64	0.87 ± 0.11
-16.10	15.96 ± 0.34	13.71 ± 0.59	0.87 ± 0.10
-15.39	15.76 ± 0.29	14.34 ± 0.54	0.90 ± 0.09
-15.14	15.77 ± 0.31	14.40 ± 0.58	0.91 ± 0.10
-15.12	15.83 ± 0.28	14.29 ± 0.53	0.91 ± 0.09
-14.18	15.61 ± 0.33	15.13 ± 0.67	0.97 ± 0.12
-14.15	15.67 ± 0.29	15.00 ± 0.57	0.97 ± 0.10
-13.32	15.44 ± 0.30	15.83 ± 0.63	1.02 ± 0.11
-13.00	15.55 ± 0.35	15.80 ± 0.73	1.04 ± 0.13
-12.67	15.43 ± 0.30	16.24 ± 0.69	1.06 ± 0.12
-12.47	15.43 ± 0.31	16.31 ± 0.72	1.07 ± 0.13
-12.30	15.32 ± 0.28	16.64 ± 0.65	1.09 ± 0.12
-12.23	15.36 ± 0.31	16.57 ± 0.70	1.09 ± 0.13
-11.29	15.21 ± 0.26	17.34 ± 0.66	1.15 ± 0.12
-11.28	15.23 ± 0.29	17.28 ± 0.72	1.15 ± 0.13
-11.26	15.17 ± 0.25	17.45 ± 0.60	1.15 ± 0.11
-10.94	15.13 ± 0.27	17.76 ± 0.66	1.18 ± 0.12
-10.32	14.98 ± 0.27	18.27 ± 0.69	1.20 ± 0.12
-10.31	14.92 ± 0.24	18.44 ± 0.66	1.20 ± 0.12
-10.29	14.99 ± 0.23	18.25 ± 0.62	1.20 ± 0.11
-9.58	14.86 ± 0.29	18.79 ± 0.80	1.23 ± 0.14
-9.35	14.69 ± 0.28	19.34 ± 0.81	1.24 ± 0.14
-9.32	14.70 ± 0.26	19.31 ± 0.76	1.24 ± 0.13
-8.36	14.34 ± 0.22	20.73 ± 0.69	1.29 ± 0.12
-8.35	14.35 ± 0.23	20.70 ± 0.71	1.29 ± 0.12
-7.38	14.16 ± 0.19	21.70 ± 0.69	1.35 ± 0.11
-7.37	14.15 ± 0.20	21.72 ± 0.67	1.35 ± 0.11
-6.49	13.90 ± 0.19	22.95 ± 0.72	1.40 ± 0.12
-6.43	14.00 ± 0.19	22.80 ± 0.66	1.42 ± 0.11
-6.40	14.03 ± 0.20	22.70 ± 0.72	1.42 ± 0.12
-6.24	13.89 ± 0.21	23.09 ± 0.81	1.42 ± 0.13
-5.46	14.06 ± 0.23	23.25 ± 0.90	1.50 ± 0.15
-5.42	14.07 ± 0.20	23.22 ± 0.72	1.51 ± 0.13
-5.36	14.24 ± 0.20	22.91 ± 0.71	1.54 ± 0.13
-4.50	13.98 ± 0.20	24.09 ± 0.80	1.58 ± 0.14
-4.49	13.96 ± 0.18	24.17 ± 0.71	1.58 ± 0.12
-4.45	14.01 ± 0.19	24.00 ± 0.69	1.58 ± 0.12
-3.56	13.84 ± 0.17	24.87 ± 0.72	1.62 ± 0.12
-3.53	13.82 ± 0.19	24.99 ± 0.77	1.62 ± 0.13
-3.52	13.90 ± 0.24	24.61 ± 1.01	1.61 ± 0.17
-3.49	13.84 ± 0.21	24.87 ± 0.89	1.62 ± 0.15
-3.34	13.89 ± 0.20	24.89 ± 0.84	1.64 ± 0.14
-1.78	13.24 ± 0.16	26.93 ± 0.74	1.59 ± 0.12
-1.50	13.19 ± 0.15	27.10 ± 0.68	1.59 ± 0.11
-0.82	12.95 ± 0.14	27.89 ± 0.68	1.56 ± 0.10
-0.57	12.86 ± 0.15	28.22 ± 0.74	1.55 ± 0.11
-0.14	12.69 ± 0.15	28.69 ± 0.75	1.52 ± 0.11
0.40	12.62 ± 0.14	28.80 ± 0.73	1.50 ± 0.10
0.88	12.58 ± 0.13	28.67 ± 0.72	1.47 ± 0.10
1.37	12.52 ± 0.14	28.51 ± 0.77	1.42 ± 0.10
2.34	12.26 ± 0.13	29.22 ± 0.74	1.37 ± 0.09
2.82	12.19 ± 0.11	29.15 ± 0.59	1.34 ± 0.07
3.03	12.11 ± 0.13	29.43 ± 0.75	1.33 ± 0.09
3.31	12.01 ± 0.11	29.76 ± 0.66	1.31 ± 0.08
4.28	11.83 ± 0.10	29.93 ± 0.64	1.25 ± 0.07
5.26	11.52 ± 0.12	31.01 ± 0.75	1.21 ± 0.08
6.22	11.30 ± 0.10	31.62 ± 0.67	1.16 ± 0.06

Table 2
(Continued)

Phase ^a (days)	Temperature T_{BB} (10^3 K)	Radius R_{BB} (10^{12} m)	Luminosity L_{BB} (10^{44} erg s ⁻¹)
6.52	11.32 ± 0.11	31.33 ± 0.75	1.15 ± 0.07
6.72	11.08 ± 0.10	32.59 ± 0.73	1.14 ± 0.07
7.19	11.10 ± 0.10	32.14 ± 0.75	1.12 ± 0.07
8.16	10.95 ± 0.10	32.50 ± 0.71	1.08 ± 0.06
8.45	10.90 ± 0.08	32.66 ± 0.56	1.07 ± 0.05
8.91	10.88 ± 0.08	32.49 ± 0.61	1.05 ± 0.05
9.13	10.83 ± 0.09	32.76 ± 0.62	1.05 ± 0.05
9.79	10.76 ± 0.07	32.82 ± 0.59	1.03 ± 0.05

Note. Temperature and radius are estimated from blackbody fitting, while luminosities are computed from fitted parameters.

^a Rest-frame days relative to the epoch of the *g*-band peak at JD 2,457,926.3.

Table 3
Summary of Optical Spectroscopy of Gaia17biu

UT Date	JD—2,457,900	Phase ^a (days)	Instrument	Exposure (s)	Slit Width (arcsec)	Wavelength Range (Å)	Resolution ($\lambda/\Delta\lambda$)
2017 May 30.9	04.41	−21.2	NOT/ALFOSC	1800	1.0	3200–9450	330
2017 May 31.9 ^b	05.38	−20.3	LT/SPRAT	350	1.8	4000–8000	350
2017 Jun 03.2	07.70	−18.1	Shane/Kast	900	2.0	3300–10600	680
2017 Jun 05.9 ^b	10.41	−15.4	LT/SPRAT	350	1.8	4000–8000	350
2017 Jun 08.0	12.48	−13.4	NOT/ALFOSC	1800	1.0	3200–9450	330
2017 Jun 10.9 ^b	15.41	−10.6	Asiago/B&C	1200	2.2	3400–9200	700
2017 Jun 10.9	15.42	−10.6	LT/SPRAT	400	1.8	4000–8000	350
2017 Jun 11.9	16.38	−9.6	Asiago/B&C	1800	2.2	3400–9200	700
2017 Jun 15.9	20.39	−5.7	LT/SPRAT	400	1.8	4000–8000	350
2017 Jun 17.2	21.68	−4.5	FLWO/FAST	900	1.5	3500–8000	1800
2017 Jun 17.9	22.43	−3.9	NOT/ALFOSC	1800	1.0	3200–9450	330
2017 Jun 19.0	23.50	−2.7	Shane/AeroSpOpIR	3600	1.1	5000–22000	600
2017 Jun 20.2	24.70	−1.6	Shane/Kast	600	2.0	3300–10600	690
2017 Jun 20.9	25.43	−0.9	LT/SPRAT	400	1.8	4000–8000	350
2017 Jun 21.0 ^b	25.46	−0.8	NOT/NotCam	3600	1.6	10000–13000	500
2017 Jun 21.2 ^c	25.67	−0.6	FLWO/FAST	900	3.0	3500–8000	1800
2017 Jun 21.2	25.70	−0.6	Shane/Kast	1800	2.0	3300–10600	690
2017 Jun 21.3	25.79	−0.5	IRTF/SpeX	540	0.5	8000–24000	100
2017 Jun 23.2	27.70	1.4	Shane/Kast	1200	1.5	3600–8200	1300
2017 Jun 24.7	28.71	2.3	Shane/Kast	1500	2.0	3500–8800	950
2017 Jun 24.9	29.41	3.0	NOT/ALFOSC	1100	1.0	3200–9450	330
2017 Jun 25.2	29.68	3.3	Shane/Kast	1800	2.0	3300–9000	710
2017 Jun 26.2	30.70	4.3	Shane/Kast	1200	2.0	3300–10600	680
2017 Jun 26.9	31.43	5.0	NOT/ALFOSC	1800	1.0	3200–9450	330
2017 Jun 27.2	31.69	5.2	Shane/Kast	1442	2.0	3300–10600	690
2017 Jun 28.2	32.71	6.2	Shane/Kast	1800	2.0	3600–10600	710
2017 Jul 01.2	35.69	9.1	Shane/Kast	750	2.0	3300–10600	690
2017 Jul 01.9	36.41	9.8	NOT/ALFOSC	1200	1.3	3200–9450	250
2017 Jul 05.2	39.69	13.0	Shane/Kast	900	2.0	3400–7800	960
2017 Jul 12.9 ^b	47.36	21.1	Asiago/B&C	1200	2.2	3400–9200	700
2017 Jul 18.2	52.68	25.6	Shane/Kast	360	2.0	3300–10600	690
2017 Jul 18.9	53.35	26.2	Asiago/AFOSC	1200	1.69	3360–7740	360

Notes.

^a Relative to the *g*-band maximum on JD 2,457,926.3.

^b This spectrum is not shown in the figures due to its low S/N.

^c This spectrum is used to estimate the host-galaxy properties but is not shown in the figures.

We thank David Sand, Carl Melis, Mike Celkins, Richard Puetter, K. Crawford, and M. Varakian for their help with some of the observations and the Lick Observatory staff for their assistance. We are grateful to Boaz Katz, Kuntal Misra, A. Gal-Yam, and S. Schulze for helpful comments.

S.B., S.D., and P.C. acknowledge Project 11573003 supported by NSFC. S.B. is partially supported by China postdoctoral science foundation grant No. 2016M600848. A.P., L.T., S.B., and N.E.R. are partially supported by the PRIN-INAF 2014 project Transient Universe: unveiling new types of stellar explosions with PESSTO. C.S.K, K.Z.S., and T.A.T. are supported by US National Science Foundation (NSF) grants AST-1515927 and AST-1515876. A.V.F.’s supernova research group at UC Berkeley is grateful for generous financial assistance from the Christopher R. Redlich Fund, the TABASGO Foundation, Gary and Cynthia Bengier (T.dj. is a Bengier Postdoctoral Fellow), and the Miller Institute for Basic Research in Science (UC Berkeley). We acknowledge support by the Ministry of Economy, Development, and Tourism’s Millennium Science Initiative through grant IC120009, awarded to the Millennium Institute of Astrophysics, MAS,

Chile (J.L.P., C.R.-C.), and from CONICYT through FONDECYT grants 3150238 (C.R.-C.) and 1151445 (J.L.P). B.J.S. is supported by NASA through Hubble Fellowship grant HST-HF-51348.001 awarded by the Space Telescope Science Institute, which is operated by the Association of Universities for Research in Astronomy, Inc., under contract NAS 5-26555. T.W.-S.H. is supported by the DOE Computational Science Graduate Fellowship, grant number DE-FG02-97ER25308. E. Y.H., C.A., S.D., and M.S., acknowledge support provided by NSF grants AST-1008343 and AST-1613472 and by the Florida Space Grant Consortium. B.S.G. and DEMONEXT were partially funded by NSF CAREER grant AST-1056524. G.H. is supported by NSF grant AST-1313484. M.D.S. is supported by a research grant (13261) from VILLUM FONDEN. NUTS is supported in part by the Instrument Centre for Danish Astrophysics (IDA). Work by S.V.Jr. is supported by NSF Graduate Research Fellowship under grant DGE-1343012. The work of N.E.R. was completed at the Institut de Ciències de l’Espai at the Autonomous University of Barcelona’s Campus; she thanks the institute for its hospitality. S.H. is supported by the Young Scholars Program of Shandong

University, Weihai. PJB’s work on SLSNe is supported by the Swift GI program through grant NNX15AR41G. J.H.W. acknowledges support by the National Research Foundation of Korea grant funded by the Korean government (No.2017R1A5A1070354). MF is supported by a Royal Society—Science Foundation Ireland University Research Fellowship. C.G. is supported by the Carlsberg Foundation.

This research was made possible through the use of the AAVSO Photometric All-Sky Survey (APASS), funded by the Robert Martin Ayers Sciences Fund. We acknowledge ESA *Gaia*, DPAC, and the Photometric Science Alerts Team (<http://gsaweb.ast.cam.ac.uk/alerts>). We thank *Swift* Acting PI S. Bradley Cenko, the Observation Duty Scientists, and the science planners for promptly approving and executing our observations. This research uses data obtained through the Telescope Access Program (TAP), which has been funded by “the Strategic Priority Research Program—The Emergence of Cosmological Structures” of the Chinese Academy of Sciences (grant No.11 XDB09000000) and the Special Fund for Astronomy from the Ministry of Finance. This work made use of the data products generated by the NYU SN group and released under [10.5281/zenodo.58766](https://doi.org/10.5281/zenodo.58766), available at <https://github.com/nyusngroup/SESNTemple/>.

Research at Lick Observatory is partially supported by a very generous gift from Google, as well as by contributions from numerous individuals, including Eliza Brown and Hal Candee, Kathy Burck and Gilbert Montoya, David and Linda Cornfield, William and Phyllis Draper, Luke Ellis and Laura Sawczuk, Alan and Gladys Hofer, Roger and Jody Lawler, DuBose and Nancy Montgomery, Jeanne and Sanford Robertson, Stanley and Miriam Schiffman, Thomas and Alison Schneider, the Hugh Stuart Center Charitable Trust, Mary-Lou Smulders and Nicholas Hodson, Clark and Sharon Winslow, Weldon and Ruth Wood, and many others. A major upgrade of the Kast spectrograph on the Shane 3 m telescope at Lick Observatory was made possible through generous gifts from William and Marina Kast, as well as the Heising-Simons Foundation.

Observations were made with the Nordic Optical Telescope, operated by the Nordic Optical Telescope Scientific Association, and with the Gran Telescopio Canarias (GTC), at the Observatorio del Roque de los Muchachos, La Palma, Spain, of the Instituto de Astrofísica de Canarias. The data presented here were obtained in part with ALFOSC, which is provided by the Instituto de Astrofísica de Andalucía (IAA) under a joint agreement with the University of Copenhagen and NOTSA.

We thank the Las Cumbres Observatory and its staff for its continuing support of the ASAS-SN project. We are grateful to M. Hardesty of the OSU ASC technology group. ASAS-SN is supported by the Gordon and Betty Moore Foundation through grant GBMF5490 to the Ohio State University and NSF grant AST-1515927. Development of ASAS-SN has been supported by NSF grant AST-0908816, the Mt. Cuba Astronomical Foundation, the Center for Cosmology and AstroParticle Physics at the Ohio State University, the Chinese Academy of Sciences South America Center for Astronomy (CASACA), the Villum Foundation, and George Skestos. This paper uses data products produced by the OIR Telescope Data Center, supported by the Smithsonian Astrophysical Observatory.

The radio observations were carried out as e-MERLIN and VLA (17A-464/AR961, 17A-470/AR962) director’s discretionary observations. e-MERLIN is a National Facility operated















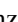




by the University of Manchester at Jodrell Bank Observatory on behalf of STFC. The National Radio Astronomy Observatory is a facility of the NSF operated under cooperative agreement by Associated Universities, Inc.

The Liverpool Telescope is operated on the island of La Palma by Liverpool John Moores University in the Spanish Observatorio del Roque de los Muchachos of the Instituto de Astrofísica de Canarias with financial support from the UK Science and Technology Facilities Council (STFC).

This work was partially based on observations collected at the Copernico telescope (Asiago, Italy) of the INAF—Osservatorio Astronomico di Padova and with the 1.22 m Galileo telescope of the Asiago Astrophysical Observatory, operated by the Department of Physics and Astronomy “G. Galilei” of the Università of Padova. This work was supported in part by the Aerospace Corporation’s Technical Investment Program.

Software: MATLAB, Python, IDL, SYNOW (Fisher et al. 1997, 1999; Branch et al. 2002), Astropy (Astropy Collaboration et al. 2013), CASA (v4.72; McMullin et al. 2007), HEASOFT (Nasa High Energy Astrophysics Science Archive Research Center (HEASARC), 2014), IRAF (Tody 1993), LT pipeline (Barnsley et al. 2012), Piascik et al. 2014), DoPHOT (Schechter et al. 1993), FOSCGUI.

ORCID iDs

Subhash Bose  <https://orcid.org/0000-0003-3529-3854>
 Subo Dong  <https://orcid.org/0000-0002-1027-0990>
 Alexei V. Filippenko  <https://orcid.org/0000-0003-3460-0103>
 C. S. Kochanek  <https://orcid.org/0000-0001-6017-2961>
 Jon Mauerhan  <https://orcid.org/0000-0002-7555-8741>
 C. Romero-Cañizales  <https://orcid.org/0000-0001-6301-9073>
 J. L. Prieto  <https://orcid.org/0000-0003-0943-0026>
 Dirk Grupe  <https://orcid.org/0000-0002-9961-3661>
 B. J. Shappee  <https://orcid.org/0000-0003-4631-1149>
 Zheng Cai  <https://orcid.org/0000-0001-8467-6478>
 E. Falco  <https://orcid.org/0000-0002-7061-6519>
 Peter Lundqvist  <https://orcid.org/0000-0002-3664-8082>
 Robert Mutel  <https://orcid.org/0000-0003-1511-6279>
 David Pooley  <https://orcid.org/0000-0003-4897-7833>
 M. D. Stritzinger  <https://orcid.org/0000-0002-5571-1833>
 S. Villanueva, Jr.  <https://orcid.org/0000-0001-6213-8804>
 Peter J. Brown  <https://orcid.org/0000-0001-6272-5507>
 E. Cappellaro  <https://orcid.org/0000-0001-5008-8619>
 Morgan Fraser  <https://orcid.org/0000-0003-2191-1674>
 Thomas de Jaeger  <https://orcid.org/0000-0001-6069-1139>
 C. Gall  <https://orcid.org/0000-0002-8526-3963>
 B. Scott Gaudi  <https://orcid.org/0000-0003-0395-9869>
 Gregory J. Herczeg  <https://orcid.org/0000-0002-7154-6065>
 T. W.-S. Holoién  <https://orcid.org/0000-0001-9206-3460>
 Griffin Hosseinzadeh  <https://orcid.org/0000-0002-0832-2974>
 E. Y. Hsiao  <https://orcid.org/0000-0003-1039-2928>
 Shaoming Hu  <https://orcid.org/0000-0003-3217-7794>
 Marie Wingyee Lau  <https://orcid.org/0000-0001-9755-9406>
 Keivan G. Stassun  <https://orcid.org/0000-0002-3481-9052>
 Stefano Valenti  <https://orcid.org/0000-0001-8818-0795>
 Jong-Hak Woo  <https://orcid.org/0000-0002-8055-5465>

References

- Angus, C. R., Levan, A. J., Perley, D. A., et al. 2016, *MNRAS*, 458, 84
 Arnaud, K. A., Branduardi-Raymont, G., Culhane, J. L., et al. 1985, *MNRAS*, 217, 105

- Asplund, M., Grevesse, N., Sauval, A. J., & Scott, P. 2009, *ARA&A*, **47**, 481
- Astropy Collaboration, Robitaille, T. P., Tollerud, E. J., et al. 2013, *A&A*, **558**, A33
- Barkat, Z., Rakavy, G., & Sack, N. 1967, *PhRvL*, **18**, 379
- Barnsley, R. M., Smith, R. J., & Steele, I. A. 2012, *AN*, **333**, 101
- Becker, R. H., White, R. L., & Helfand, D. J. 1995, *ApJ*, **450**, 559
- Berdugina, A., Pirola, V., & Teerikorpi, P. 2014, *A&A*, **561**, A24
- Bietenholz, M. F., De Colle, F., Granot, J., Bartel, N., & Soderberg, A. M. 2014, *MNRAS*, **440**, 821
- Blinnikov, S. I., & Sorokina, E. I. 2010, arXiv:1009.4353
- Blondin, S., & Tonry, J. L. 2007, *ApJ*, **666**, 1024
- Bodenheimer, P., & Ostriker, J. P. 1974, *ApJ*, **191**, 465
- Branch, D., Benetti, S., Kasen, D., et al. 2002, *ApJ*, **566**, 1005
- Breeveld, A. A., Landsman, W., Holland, S. T., et al. 2011, in AIP Conf. Ser. 1358, ed. J. E. McEnery, J. L. Racusin, & N. Gehrels (Melville, NY: AIP), 373
- Brown, P. J., Yang, Y., Cooke, J., et al. 2016, *ApJ*, **828**, 3
- Brown, T. M., Baliber, N., Bianco, F. B., et al. 2013, *PASP*, **125**, 1031
- Bruzual, G., & Charlot, S. 2003, *MNRAS*, **344**, 1000
- Burrows, D. N., Hill, J. E., Nousek, J. A., et al. 2005, *SSRv*, **120**, 165
- Chabrier, G. 2003, *PASP*, **115**, 763
- Chatzopoulos, E., Wheeler, J. C., Vinko, J., Horvath, Z. L., & Nagy, A. 2013, *ApJ*, **773**, 76
- Chen, T.-W., Nicholl, M., Smartt, S. J., et al. 2017a, *A&A*, **602**, A9
- Chen, T.-W., Smartt, S. J., Bresolin, F., et al. 2013, *ApJL*, **763**, L28
- Chen, T.-W., Smartt, S. J., Yates, R. M., et al. 2017b, *MNRAS*, **470**, 3566
- Dai, Z. G., Wang, S. Q., Wang, J. S., Wang, L. J., & Yu, Y. W. 2016, *ApJ*, **817**, 132
- De Cia, A., Gal-Yam, A., Rubin, A., et al. 2017, *ApJ*, submitted (arXiv:1708.01623)
- Delgado, A., Harrison, D., Hodgkin, S., et al. 2017, *TNSTR*, 591
- Dong, S., Bose, S., Chen, P., et al. 2017, *ATel*, 10498
- Dong, S., Shappee, B. J., Prieto, J. L., et al. 2016, *Sci*, **351**, 257
- Dwarkadas, V. V., & Gruszko, J. 2012, *MNRAS*, **419**, 1515
- Fabricant, D., Cheimets, P., Caldwell, N., & Geary, J. 1998, *PASP*, **110**, 79
- Filippenko, A. V. 1982, *PASP*, **94**, 715
- Fisher, A., Branch, D., Hatano, K., & Baron, E. 1999, *MNRAS*, **304**, 67
- Fisher, A., Branch, D., Nugent, P., & Baron, E. 1997, *ApJL*, **481**, L89
- Galama, T. J., Vreeswijk, P. M., van Paradijs, J., et al. 1998, *Natur*, **395**, 670
- Gal-Yam, A. 2012, *Sci*, **337**, 927
- Gehrels, N., Chincarini, G., Giommi, P., et al. 2004, *ApJ*, **611**, 1005
- Godoy-Rivera, D., Stanek, K. Z., Kochanek, C. S., et al. 2017, *MNRAS*, **466**, 1428
- Grupe, D., Dong, S., Prieto, J. L., & Pooley, D. 2017a, *ATel*, 10499
- Grupe, D., Dong, S., Prieto, J. L., & Pooley, D. 2017b, *ATel*, 10531
- Hill, J. E., Burrows, D. N., Nousek, J. A., et al. 2004, *Proc. SPIE*, **5165**, 217
- Hoflich, P. 1991, *A&A*, **246**, 481
- Holoien, T. W.-S., Brown, J. S., Stanek, K. Z., et al. 2017a, *MNRAS*, **471**, 4966
- Holoien, T. W.-S., Brown, J. S., Stanek, K. Z., et al. 2017b, *MNRAS*, **467**, 1098
- Holoien, T. W.-S., Kochanek, C. S., Prieto, J. L., et al. 2016, *MNRAS*, **455**, 2918
- Hu, S.-M., Han, S.-H., Guo, D.-F., & Du, J.-J. 2014, *RAA*, **14**, 719
- Huber, M., Chambers, K. C., Flewelling, H., et al. 2015, *ATel*, 7153
- Insera, C., Bulla, M., Sim, S. A., & Smartt, S. J. 2016, *ApJ*, **831**, 79
- Insera, C., & Smartt, S. J. 2014, *ApJ*, **796**, 87
- Insera, C., Smartt, S. J., Jerkstrand, A., et al. 2013, *ApJ*, **770**, 128
- Kalberla, P. M. W., Burton, W. B., Hartmann, D., et al. 2005, *A&A*, **440**, 775
- Kangas, T., Blagorodnova, N., Mattila, S., et al. 2017, *MNRAS*, **469**, 1246
- Kasen, D., & Bildsten, L. 2010, *ApJ*, **717**, 245
- Kelly, P. L., & Kirshner, R. P. 2012, *ApJ*, **759**, 107
- Kewley, L. J., & Ellison, S. L. 2008, *ApJ*, **681**, 1183
- Kraft, R. P., Burrows, D. N., & Nousek, J. A. 1991, *ApJ*, **374**, 344
- Kriek, M., van Dokkum, P. G., Labbé, I., et al. 2009, *ApJ*, **700**, 221
- Law, N. M., Kulkarni, S. R., Dekany, R. G., et al. 2009, *PASP*, **121**, 1395
- Leaman, J., Li, W., Chornock, R., & Filippenko, A. V. 2011, *MNRAS*, **412**, 1419
- Leloudas, G., Fraser, M., Stone, N. C., et al. 2016, *NatAs*, **1**, 0002
- Leloudas, G., Maund, J. R., Gal-Yam, A., et al. 2017, *ApJL*, **837**, L14
- Leloudas, G., Patat, F., Maund, J. R., et al. 2015a, *ApJL*, **815**, L10
- Leloudas, G., Schulze, S., Krühler, T., et al. 2015b, *MNRAS*, **449**, 917
- Levinson, A., Ofek, E. O., Waxman, E., & Gal-Yam, A. 2002, *ApJ*, **576**, 923
- Liu, Y.-Q., Modjaz, M., & Bianco, F. B. 2017, *ApJ*, **845**, 85
- Lunnan, R., Chornock, R., Berger, E., et al. 2013, *ApJ*, **771**, 97
- Lunnan, R., Chornock, R., Berger, E., et al. 2014, *ApJ*, **787**, 138
- Lunnan, R., Chornock, R., Berger, E., et al. 2015, *ApJ*, **804**, 90
- Lunnan, R., Chornock, R., Berger, E., et al. 2016, *ApJ*, **831**, 144
- Lunnan, R., Chornock, R., Berger, E., et al. 2018, *ApJ*, **852**, 81
- Lunnan, R., Kasliwal, M. M., Cao, Y., et al. 2017, *ApJ*, **836**, 60
- Margutti, R., Kamble, A., Milisavljevic, D., et al. 2017a, *ApJ*, **835**, 140
- Margutti, R., Metzger, B. D., Chornock, R., et al. 2017b, *ApJ*, **836**, 25
- Margutti, R., Soderberg, A. M., Wieringa, M. H., et al. 2013, *ApJ*, **778**, 18
- Massey, P., & Gronwall, C. 1990, *ApJ*, **358**, 344
- Massey, P., Strobel, K., Barnes, J. V., & Anderson, E. 1988, *ApJ*, **328**, 315
- Mattila, S., Elias-Rosa, N., Lundqvist, P., et al. 2016, *ATel*, 8992
- Mauerhan, J., Williams, G. G., Smith, N., et al. 2014, *MNRAS*, **442**, 1166
- Mauerhan, J. C., Williams, G. G., Leonard, D. C., et al. 2015, *MNRAS*, **453**, 4467
- McCrum, M., Smartt, S. J., Kotak, R., et al. 2014, *MNRAS*, **437**, 656
- McCrum, M., Smartt, S. J., Rest, A., et al. 2015, *MNRAS*, **448**, 1206
- McMullin, J. P., Waters, B., Schiebel, D., Young, W., & Golap, K. 2007, in ASP Conf. Ser. 376, *Astronomical Data Analysis Software and Systems XVI*, ed. R. A. Shaw, F. Hill, & D. J. Bell (San Francisco, CA: ASP), 127
- Miller, J., & Stone, R. 1993, *Lick Obs. Tech. Rep.* 66
- Nagao, T., Maiolino, R., & Marconi, A. 2006, *A&A*, **459**, 85
- Nasa High Energy Astrophysics Archive Research Center (HEASARC) 2014, *HEASoft: Unified Release of FTOOLS and XANADU*, Astrophysics Source Code Library, ascl:1408.004
- Neill, J. D., Sullivan, M., Gal-Yam, A., et al. 2011, *ApL*, **727**, 15
- Nicholl, M., Berger, E., Margutti, R., et al. 2017, *ApJL*, **845**, L8
- Nicholl, M., Berger, E., Smartt, S. J., et al. 2016, *ApJ*, **826**, 39
- Nicholl, M., & Smartt, S. J. 2016, *MNRAS*, **457**, L79
- Nicholl, M., Smartt, S. J., Jerkstrand, A., et al. 2013, *Natur*, **502**, 346
- Nicholl, M., Smartt, S. J., Jerkstrand, A., et al. 2015a, *ApJL*, **807**, L18
- Nicholl, M., Smartt, S. J., Jerkstrand, A., et al. 2015b, *MNRAS*, **452**, 3869
- Pastorello, A., Smartt, S. J., Botticella, M. T., et al. 2010, *ApJL*, **724**, L16
- Perley, D. A., Quimby, R. M., Yan, L., et al. 2016, *ApJ*, **830**, 13
- Pettini, M., & Pagel, B. E. J. 2004, *MNRAS*, **348**, L59
- Piascik, A. S., Steele, I. A., Bates, S. D., et al. 2014, *Proc. SPIE*, **9147**, 91478H
- Planck Collaboration, Ade, P. A. R., Aghanim, N., et al. 2016, *A&A*, **594**, A13
- Prajs, S., Sullivan, M., Smith, M., et al. 2017, *MNRAS*, **464**, 3568
- Prieto, J. L., Stanek, K. Z., & Beacom, J. F. 2008, *ApJ*, **673**, 999
- Quimby, R. M., Aldering, G., Wheeler, J. C., et al. 2007, *ApJL*, **668**, L99
- Quimby, R. M., Kulkarni, S. R., Kasliwal, M. M., et al. 2011, *Natur*, **474**, 487
- Quimby, R. M., Yuan, F., Akerlof, C., & Wheeler, J. C. 2013, *MNRAS*, **431**, 912
- Rayner, J. T., Toomey, D. W., Onaka, P. M., et al. 2003, *PASP*, **115**, 362
- Romero-Canizales, C., Beswick, R., Dong, S., & Prieto, J. L. 2017, *ATel*, 10537
- Roming, P. W. A., Kennedy, T. E., Mason, K. O., et al. 2005, *SSRv*, **120**, 95
- Schechter, P. L., Mateo, M., & Saha, A. 1993, *PASP*, **105**, 1342
- Schlafly, E. F., & Finkbeiner, D. P. 2011, *ApJ*, **737**, 103
- Schulze, S., Krühler, T., Leloudas, G., et al. 2018, *MNRAS*, **473**, 1258
- SDSS Collaboration, Albareti, F. D., Allende Prieto, C., et al. 2017, *ApJS*, **233**, 25
- Serkowski, K., Mathewson, D. S., & Ford, V. L. 1975, *ApJ*, **196**, 261
- Shappee, B. J., Prieto, J. L., Grupe, D., et al. 2014, *ApJ*, **788**, 48
- Silverman, J. M., Foley, R. J., Filippenko, A. V., et al. 2012, *MNRAS*, **425**, 1789
- Skrutskie, M. F., Cutri, R. M., Stiening, R., et al. 2006, *AJ*, **131**, 1163
- Soderberg, A. M., Chakraborti, S., Pignatta, G., et al. 2010, *Natur*, **463**, 513
- Soderberg, A. M., Kulkarni, S. R., Berger, E., et al. 2004, *Natur*, **430**, 648
- Soderberg, A. M., Kulkarni, S. R., Nakar, E., et al. 2006, *Natur*, **442**, 1014
- Sorokina, E., Blinnikov, S., Nomoto, K., Quimby, R., & Tolstov, A. 2016, *ApJ*, **829**, 17
- Stanek, K. Z., Gnedin, O. Y., Beacom, J. F., et al. 2006, *AcA*, **56**, 333
- Stoll, R., Prieto, J. L., Stanek, K. Z., et al. 2011, *ApJ*, **730**, 34
- Stoll, R., Prieto, J. L., Stanek, K. Z., & Pogge, R. W. 2013, *ApJ*, **773**, 12
- Tody, D. 1993, in ASP Conf. Ser. 52, *Astronomical Data Analysis Software and Systems II*, ed. R. J. Hanisch, R. J. V. Brissenden, & J. Barnes (San Francisco, CA: ASP), 173
- Tremonti, C. A., Heckman, T. M., Kauffmann, G., et al. 2004, *ApJ*, **613**, 898
- Villanueva, S., Eastman, J. D., Gaudi, B. S., et al. 2016, *Proc. SPIE*, **9906**, 99062L
- Woosley, S. E. 2010, *ApJL*, **719**, L204
- Woosley, S. E., Blinnikov, S., & Heger, A. 2007, *Natur*, **450**, 390
- Xiang, D., Song, H., Wang, X., et al. 2017, *ATel*, 10442
- Yan, L., Quimby, R., Gal-Yam, A., et al. 2017, *ApJ*, **840**, 57
- Yaron, O., & Gal-Yam, A. 2012, *PASP*, **124**, 668
- Yates, R. M., Kauffmann, G., & Guo, Q. 2012, *MNRAS*, **422**, 215